Physics of Fluids

RESEARCH ARTICLE | SEPTEMBER 21 2023

# Blockage ratio and Reynolds number effects on flows around a rectangular prism

Fati Bio Abdul-Salam ; Xingjun Fang (方兴军) ; Mark Francis Tachie



*Physics of Fluids* 35, 095137 (2023)
https://doi.org/10.1063/5.0165627





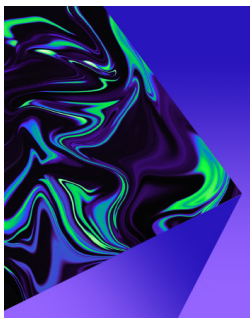

Physics of Fluids ARTICLE pubs.aip.org/aip/pof

# Blockage ratio and Reynolds number effects on flows around a rectangular prism

Cite as: Phys. Fluids **35**, 095137 (2023); doi: 10.1063/5.0165627
Submitted: 29 June 2023 · Accepted: 29 August 2023 ·
Published Online: 21 September 2023



Fati Bio Abdul-Salam,[1,a)] Xingjun Fang (方兴军),[1,2] and Mark Francis Tachie[1]

## AFFILIATIONS

[1]Department of Mechanical Engineering, University of Manitoba, Winnipeg, Manitoba R3T 5V6, Canada
[2]Institute of Mechanics, Chinese Academy of Sciences, Beijing, 100190, People's Republic of China

[a)]Author to whom correspondence should be addressed: abdulsa8@myumanitoba.ca

## ABSTRACT

The combined effects of blockage ratio (*BR*) and Reynolds number (Re) on the spatiotemporal characteristics of turbulent flow separation around a rectangular prism with depth-to-thickness ratio of 3 were investigated using a time-resolved particle image velocimetry. Four different blockage ratios ($BR = 2.5\%$, 5%, 10%, and 15%) were examined at Reynolds numbers of 3000, 7500, and 15000. Two regimes (unattached and reattached) were identified; however, the boundary between these regimes shows a complex dependency on *BR* and Re. The mean flow does not reattach onto the prism at low *BR* and Re but tends to reattach when *BR* and Re increase. The wake vortices are relatively larger for the unattached test cases. The separation bubbles over and in the wake of the prism are dynamically coupled for prisms in the unattached regime but independent of each other in the reattached regime. Spectral analyses of the velocity fluctuations and coefficient of the first proper orthogonal decomposition mode pair reveal a single dominant peak at the same fundamental shedding frequency for the reattached test cases, whereas multiple competing frequencies are observed for test cases in the unattached regime. The Kelvin–Helmholtz frequency increases with an increase in *BR* and Re. The vortical structures are more organized for prisms in the reattached regime, and their convective velocities in the wake are comparatively higher.





## I. INTRODUCTION

Separating flow past sharp-edged rectangular prisms is a canonical test case that has drawn significant research attention over the past decades (Bearman and Trueman, 1972; Okajima, 1982; Durão *et al.*, 1988; Lyn *et al.*, 1995; and Shadaram *et al.*, 2008) and remains an active research topic (Trias *et al.*, 2015; Alves Portela *et al.*, 2017; Bai and Alam, 2018; and Kumahor and Tachie, 2022). The flow is exemplified by both a small-scale Kelvin–Helmholtz (KH) instability, which originates from the roll up of the separated shear layers formed at the leading edges, and a large-scale vortex shedding, which manifests as a train of alternating signed large-scale vortices that are convected in the downstream direction. One can detect the KH vortices downstream of their point of formation owing to their convective nature, as broadband high frequency peaks in the frequency spectra of the fluctuating velocities (Brun *et al.*, 2008; Lander *et al.*, 2018; and Moore *et al.*, 2019a). The large-scale vortex shedding, on the other hand, has a global signature and is detectable both upstream and downstream of their origin at frequencies that are comparatively lower than the frequency of the KH instability (Lander *et al.*, 2018; Moore *et al.*, 2019a; and Kumahor and Tachie, 2023). In spite of their geometric simplicity, the dynamics of separated flows around rectangular prisms are complicated by the co-existence and nonlinear interaction of these instabilities with distinctive length and time scales, as well as unique features such as streamline curvature, pressure gradients, and massive unsteady recirculation region. These flow characteristics are also of considerable relevance in diverse engineering and environmental applications. For instance, the large-scale periodic vortex shedding contributes to unsteady aerodynamic loads on engineering structures, resulting in vortex-induced vibration and fatigue failure (Cermak, 1976; Park and Yang, 2016). Prediction and mitigation of these adverse effects underscore the need to understand the spatiotemporal characteristics of separating flows induced by rectangular prisms.

A schematic of a two-dimensional rectangular prism in a uniform flow is shown in Fig. 1(a). Previous investigations (Okajima, 1982; Bai and Alam, 2018; Moore *et al.*, 2019a; and Liu *et al.*, 2023) have demonstrated that the flow characteristics are significantly affected by Reynolds number ($\mathrm{Re} = U_e h/\nu$, where $U_e$ is the incoming velocity, $h$ is the body thickness, and $\nu$ is the kinematic viscosity), depth-to-thickness ratio ($d/h$, where d is the streamwise depth of the body), and turbulence intensity. At low Reynolds numbers ($\mathrm{Re} < 120$),

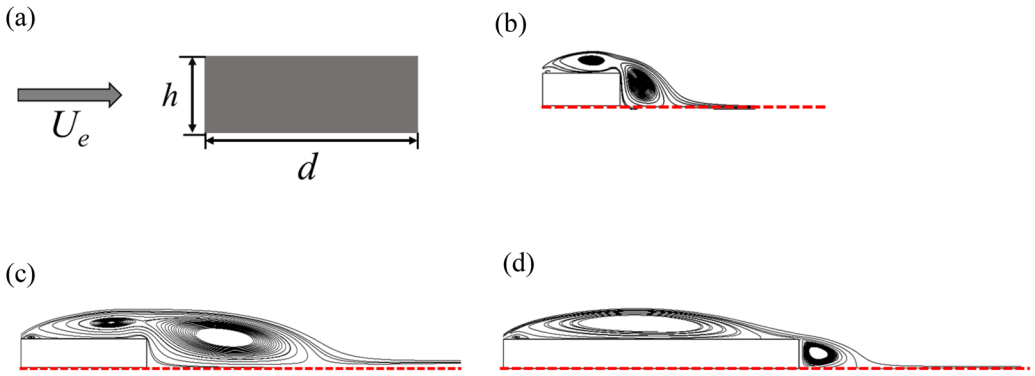


**FIG. 1.** (a) Schematic of a two-dimensional rectangular prism at zero incidence to a uniform flow and the mean flow topologies over (b) a short prism ($d/h = 1$), (c) an intermediate prism ($d/h = 2$), and (d) a long prism ($d/h = 4$). The dashed lines in (b)–(d) are the lines of symmetry.

the flow evolves around the rectangular prism and separates at the trailing edge to form the von Kármán (VK) vortex street in the wake region. However, the separating point shifts to the leading edge at $\mathrm{Re} > 120$ irrespective of the depth-to-thickness ratio (Robichaux *et al.*, 1999; Yoon *et al.*, 2010; Bai and Alam, 2018; and Mashhadi *et al.*, 2021). The depth-to-thickness ratio of a rectangular prism has profound effects on the drag characteristics (Davis *et al.*, 1984; Norberg, 1993; Yu *et al.*, 2013; Mohebi *et al.*, 2017; and Kumahor and Tachie, 2022), flow topology (Moore *et al.*, 2019a; Kumahor and Tachie, 2022; and Liu *et al.*, 2023), shedding frequency (Okajima, 1982; Igarashi, 1985; Norberg, 1993; Moore *et al.*, 2019a; and Kumahor and Tachie, 2022), and proximity of KH and VK instabilities (Moore *et al.*, 2019a; Kumahor and Tachie, 2023). Indeed, based on the depth-to-thickness ratio, three distinct regimes can be observed: short prisms, intermediate prisms, and long prisms. For short prisms ($d/h < 2$), the separated flow is shed directly into the wake region behind the prism [see Fig. 1(b)], for intermediate prisms ($2 \leq d/h < 3.5$), the separated shear layer reattaches intermittently onto the surface of the prism [see Fig. 1(c)], and for long prisms ($d/h \geq 3.5$), the shear layer reattaches onto the surface of the prism [see Fig. 1(d)]. The exact $d/h$ demarcating these regimes are not universal due to the sensitivity of the shear layer to external influences such as Reynolds number, turbulence intensity, and blockage ratio.

The effects of Reynolds number on vortex shedding and drag characteristics have been critically examined for a wide range of depth-to-thickness ratios (0.05–8.0). Selected investigations are summarized in Table I. For short and long prisms, previous investigations have shown that for $\mathrm{Re} > 1000$, both the drag coefficient and the dominant shedding frequency are independent of Reynolds number (Okajima, 1982; Igarashi, 1985; Norberg, 1993; Brun *et al.*, 2008; Bai and Alam, 2018; Lander *et al.*, 2018; and Moore *et al.*, 2019a). On the other hand, the shear layer frequency (KH) increases with increasing Reynolds number. Lander *et al.* (2018) examined the influence of Reynolds number on the frequency scaling for a square prism ($d/h = 1$) and proposed the following relation $f_{KH}/f_{VK} = 0.18Re^{0.60}$. Moore *et al.* (2019a) also investigated the scaling frequency of short and long prisms ($d/h = 1$ and 5) and observed that the frequency ratio ($f_{KH}/f_{VK}$) is comparatively higher for the short prism. This observation suggests that the degree of interaction between the small-scale KH instability and the large-scale von Kármán vortices depends not only on the Reynolds number but also on the depth-to-thickness ratio.

Okajima (1982) investigated the Strouhal number ($St = fh/U_e$, which is the dimensionless shedding frequency) of rectangular prisms ($d/h = 1$, 2, 3, and 4) over a Reynolds number range of 70–20 000. They showed that for prisms in the intermediate regime ($d/h = 2$ and

**TABLE I.** Summary of key parameters from previous pertinent studies in the literature.

| Authors | Re | *BR* (%) | *d*/*h* | *St* |
|---|---|---|---|---|
| Okajima (1982) | 70–20 000 | 1.0–7.5 | 1 | 0.10–0.15 |
| | | | 2 | 0.06–0.17 |
| | | | 3 | 0.03–0.17 |
| | | | 4 | 0.13–0.14 |
| Igarashi (1986) | 3850–15 400 | 2.5 | 2 | 0.07–0.08 |
| | | | 2.5 | 0.06–0.12 |
| | | | 2.8 | 0.13–0.17 |
| | | | 3 | 0.14–0.16 |
| | | | 4 | 0.13–0.14 |
| Norberg (1993) | 400–30 000 | 1.5–4.7 | 1 | 0.12–0.15 |
| | | | 2 | 0.05–0.16 |
| | | | 2.5 | 0.05–0.19 |
| | | | 3 | 0.05–0.18 |
| Yu and Kareem (1998) | 100 000 | 5.9 | 1 | 0.14 |
| | | | 1.5 | 0.11 |
| | | | 2 | 0.09 |
| | | | 3 | 0.19 |
| | | | 4 | 0.16 |
| Nakagawa *et al.* (1999) | 3000 | 20.0 | 0.5 | 0.15 |
| | | | 1 | 0.13 |
| | | | 2 | 0.19 |
| | | | 3 | 0.20 |
| Moore *et al.* (2019a) | 13 400–118 000 | 6.4 | 1 | 0.13 |
| | | | 3 | 0.15 |
| | | | 5 | 0.11 |
| Kumahor and Tachie (2022) | 16 200 | 7.0 | 1 | 0.14 |
| | | | 5 | 0.11 |

3), there is a sudden discontinuity in $St$ due to changes in flow pattern. In this regime, two significant frequencies were observed for a Reynolds number range of 500–600 with $d/h = 2$ and 1000–3000 with $d/h = 3$. However, with a further increase in Reynolds number, only one dominant frequency was observed. They attributed the occurrence of dual frequencies to intermittent flow reattachment. Norberg (1993) also studied the flow around rectangular prisms with varying depth-to-thickness ratios ($d/h = 1$–5) over a Reynolds number range of 400–30 000. They observed double and even triple dominant frequencies for prisms in the intermediate regime for Reynolds number range of 500–25 000 ($d/h = 2$) and 600–4000 ($d/h = 3$). It is evident that the flow dynamics, particularly the Strouhal number, for prisms in the intermediate regime are quite sensitive to Reynolds number. It should be noted that these experimental investigations (Okajima, 1982; Norberg, 1993) were performed using hot-wire anemometry, and due to the high local turbulence levels within the wake, the measurements were performed in the outer part of the near-wake region. Norberg (1993) remarked that the appearance of the dominant peaks in the near-wake region depended on the measurement position and probably explains the difference between the number of peaks observed in his study compared to that of Okajima (1982).

Rectangular prisms in the intermediate regime are complex and sensitive to the incoming boundary condition. There exists significant scatter in the literature in the flow characteristics for prisms in this regime even at similar Reynolds numbers. For instance, Nakagawa *et al.* (1999) reported mean flow reattachment for the $d/h = 3$ prism at $BR$ ($= h/W$, where $W$ is the tunnel width) of 20%, whereas the study by Liu *et al.* (2023) at $BR = 7\%$ did not show mean flow reattachment even though both investigations were carried out at the same Reynolds number ($\mathrm{Re} = 3000$). Also, for the $d/h = 3$ prism, the study by Moore *et al.* (2019a) at $BR = 6.4\%$ and Moore *et al.* (2019b) at $BR = 7.2\%$ for similar Reynolds number showed mean flow reattachment in the latter and not in the former. This suggests that prisms in the intermediate regime are not only sensitive to Reynolds number, but blockage ratio may also have significant effects. We also observed in the literature that these discrepancies are mostly attributed to differences in blockage ratio among studies (Nakagawa *et al.*, 1999; Shadaram *et al.*, 2008; and Mashhadi *et al.*, 2021); however, the influence of blockage ratio for prisms in the intermediate regime has not yet been deliberately investigated. Therefore, the objective of the present study is to critically examine the effects of blockage ratio and Reynolds number on the spatiotemporal characteristics of separating flows induced by a rectangular prism with an intermediate depth-to-thickness ratio ($d/h = 3$). The rest of the paper is organized as follows: experimental details are provided in Sec. II, followed by results and discussion in Secs. III and IV.

## II. EXPERIMENTAL SETUP AND METHODOLOGY

The experiments were performed using a time-resolved particle image velocimetry (PIV) in an open recirculating water channel located in the Turbulence and Hydraulic Engineering Laboratory (THEL) at the University of Manitoba. The test section has interior dimensions of length 6000 mm, width 600 mm, and height 450 mm. To allow optical access to the flow, the side and bottom walls of the test section are made from smooth transparent Abrasion Resistant® acrylic plates. A 30 kW pump is used to drive the recirculating water.

Table II provides a summary of the test parameters used in the present experimental study. As shown in the table, a total of ten test cases from a combination of blockage ratios and Reynolds numbers were examined. For conciseness, a notation is constructed from both the blockage ratio and Reynolds number for the various test cases. For instance, $R_3B_5$ refers to test case at $\mathrm{Re} = 3000$ and $BR = 5\%$. The inclusion of superscript "*" in the notation of certain test cases is used to differentiate those with mean flow reattachment onto the surface of the prism from those that do not reattach, which will be further explained in the discussion section. For each prism, the streamwise depth ($d$) was three times the thickness ($h$). To investigate the effects of blockage ratios for a given Reynolds number, the thicknesses of the prisms and channel width were varied. For blockage ratios 2.5% and 5%, the thicknesses of the prisms were 15 and 30 mm, respectively, and the channel width was 600 mm. A false wall was created using a 9 mm thick transparent acrylic plate and screwed firmly to the base of the section to reduce the width of the test section from 600 to 300 mm. For blockage ratios 10% and 15%, the thicknesses of the prisms were 30 and 45 mm, respectively. The water depth ($H$) in the test section was 430 mm. The velocity of the water was varied from 0.07 to 0.50 m/s to achieve the designated Reynolds numbers. The prisms were mounted upright at the center of the channel width. The vertical height ($B$) of the prisms was 580 mm for all test cases.

A time-resolved particle image velocimetry (TR-PIV) system was used for the velocity measurements. The water was seeded with 10 $\mu$m silver coated hollow glass spheres, which have a density of 1400 kg/m$^3$.

**TABLE II.** Summary of test cases and the associated notations.

| $U_e$ (m/s) | $h$ (mm) | $W$ (mm) | Re | $BR$ (%) | FOV$_1$ ($x/h \times y/h$) | FOV$_2$ ($x/h \times y/h$) | Notation |
|---|---|---|---|---|---|---|---|
| 0.20 | 15 | 600 | 3000 | 2.5 | 8.0 × 5.1 | 11.5 × 7.2 | $R_3B_{2.5}$ |
| 0.10 | 30 | 600 | 3000 | 5 | 4.0 × 2.5 | 5.8 × 3.6 | $R_3B_5$ |
| 0.10 | 30 | 300 | 3000 | 10 | 4.1 × 2.6 | 7.8 × 4.8 | $R_3B_{10}^*$ |
| 0.07 | 45 | 300 | 3000 | 15 | 2.8 × 1.7 | 5.2 × 3.2 | $R_3B_{15}^*$ |
| 0.50 | 15 | 600 | 7500 | 2.5 | 8.0 × 5.1 | 11.5 × 7.2 | $R_7B_{2.5}$ |
| 0.25 | 30 | 600 | 7500 | 5 | 4.0 × 2.5 | 5.8 × 3.6 | $R_7B_5^*$ |
| 0.25 | 30 | 300 | 7500 | 10 | 4.1 × 2.6 | 7.8 × 4.8 | $R_7B_{10}^*$ |
| 0.17 | 45 | 300 | 7500 | 15 | 2.8 × 1.7 | 5.2 × 3.2 | $R_7B_{15}^*$ |
| 0.50 | 30 | 600 | 15 000 | 5 | 4.0 × 2.5 | 5.8 × 3.6 | $R_{15}B_5$ |
| 0.33 | 45 | 300 | 15 000 | 15 | 2.8 × 1.7 | 5.2 × 3.2 | $R_{15}B_{15}^*$ |

The relaxation time of the seeding particles was estimated using the following equation:

$$\tau_p = \frac{{d_p}^2(\rho_p - \rho_f)}{18\rho_f \nu}, \quad (1)$$

where $d_p$ is the diameter of the seeding particles, $\nu$ is the kinematic viscosity, while $\rho_f$ and $\rho_p$ are the densities of water and seeding particles, respectively. The value of the relaxation time was calculated to be $2.2 \times 10^{-6}$ s. The smallest time scale ($\tau_\eta$) was approximately $4.90 \times 10^{-4}$ s according to $\tau_\eta = Re^{-1/2} \times \tau_o$, where ($\tau_o = h/U_e$) is the largest time scale in the flow (Pope, 2000). Therefore, the Stokes number ($S_k = \tau_p/\tau_\eta$) was $4.59 \times 10^{-3}$, which is lower than the recommended threshold of 0.05 (Samimy and Lele, 1991). The seeding particles used in the present study, therefore, followed the flow of the local fluid velocity faithfully.

A diode pumped dual-cavity high-speed neodymium-doped yttrium lithium fluoride (Nd:YLF) laser with maximum pulse energy of 30 mJ/pulse for each cavity was used to illuminate the flow field. Figure 2 shows the schematic of the experimental setup. The measurement plane was at half water depth ($H/2$). An acrylic surface plate was immersed 2mm into the water to calm the free surface. The light scattered from the particles was captured using two high-speed 12-bit complementary metal oxide semiconductor (CMOS) cameras of resolution 2560 pixels × 1600 pixels. The cameras were placed above the test section and positioned side-by-side to capture the particle images. The first camera was fitted with a Sigma 105 mm lens, and the second camera was fitted with a Nikon 60 mm lens, both capturing simultaneous images of the illuminated seeding particles in $FOV_1$ and $FOV_2$, respectively. There was a 15 mm overlap in the streamwise direction between these two fields of view. The dimensions of $FOV_1$ and $FOV_2$ for each test case are summarized in Table II. For each test case, 60 000 snapshots of velocity fields were acquired at a sampling rate of 800 Hz.

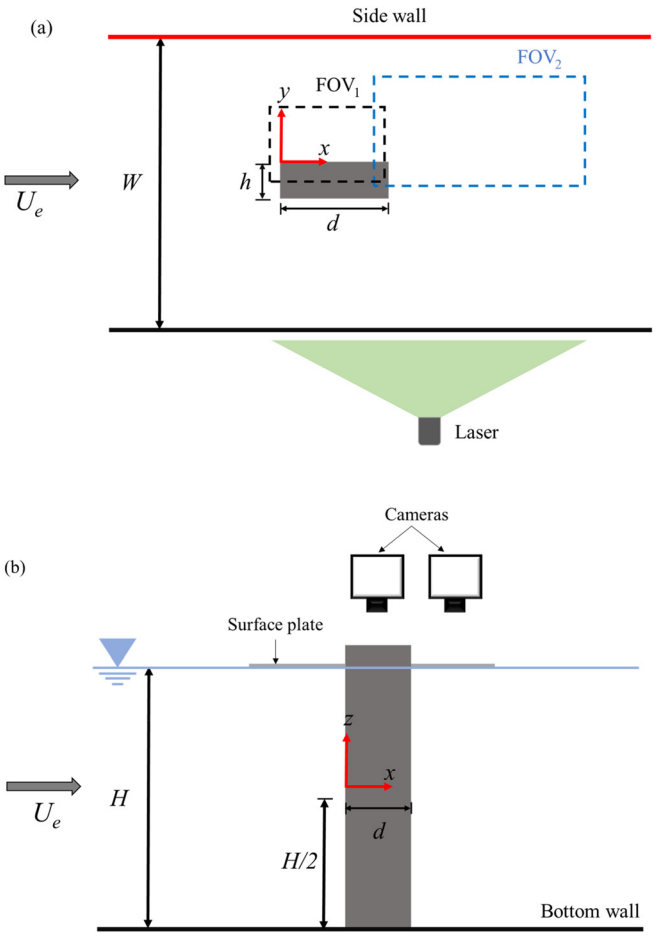


**FIG. 2.** Schematic of the experimental setup (not to scale) in the (a) top and (b) side views as well as the adopted coordinate system and nomenclature.

A commercial software (DaVis version 10) was used for data acquisition, image processing, and vector calculations. The velocity vectors were calculated using a graphical processing unit (GPU) accelerated multi-pass cross correlation algorithm. The initial interrogation area was 128 pixels × 128 pixels with 50% overlap. This was followed by four final passes with an interrogation area of 24 pixels × 24 pixels with 75% overlap. For $FOV_1$, the vector spacing was 0.29 mm for both setups. Meanwhile, the vector spacings for $FOV_2$ were 0.45 and 0.55 mm for test cases without a false wall ($BR = 2.5\%$ and 5%) and with false wall ($BR = 10\%$ and 15%), respectively. The instantaneous velocity vectors were post-processed using in-house MATLAB® scripts. Uncertainty analysis of the present PIV measurements was performed using the framework outlined in Sciacchitano and Wieneke (2016). The measurement uncertainties for the mean velocity and Reynolds normal stresses were less than 3% and 5%, respectively, at a 95% confidence level.

## III. RESULTS AND DISCUSSION

For brevity, only selected test cases are presented to highlight the influence of blockage ratio and Reynolds number. For a given Reynolds number, two test cases at different blockage ratios are presented to represent the unattached and reattached regimes. Additionally, data presentation is limited to only one side of the centerline for conciseness, because the turbulence statistics are symmetric about the centerline of the prism for all the tests cases.

### A. Mean flow characteristics

Figure 3 shows the mean flow fields for six cases ($R_3B_5$, $R_3B_{10}{}^*$, $R_7B_{2.5}$, $R_7B_5{}^*$, $R_{15}B_5$, and $R_{15}B_{15}{}^*$) selected to illustrate the effects of blockage ratio and Reynolds number. In general, the incoming flow separates at the sharp leading edge of the prism and deflects into the uniform flow. Distinct recirculation bubbles referred to as primary and wake vortices are formed over and in the wake of the prisms, respectively. A comparatively small secondary recirculation bubble is formed in the proximity of the leading edge due to an adverse pressure gradient caused by the deceleration of the reverse flow near the leading edge (Cimarelli *et al.*, 2018). At low blockage ratios and/or Reynolds numbers [Figs. 3(a), 3(c), and 3(e)], the mean flow does not reattach onto the prism but is drawn into the wake. As shown in the animation in Fig. 4 (Multimedia view), the flow topology in these cases is reminiscent of intermittent detachment and reattachment observed for prisms in the intermediate regime [see Fig. 1(c)]. As the blockage ratio and/or Reynolds number increase [Figs. 3(b), 3(d), and 3(f)], the

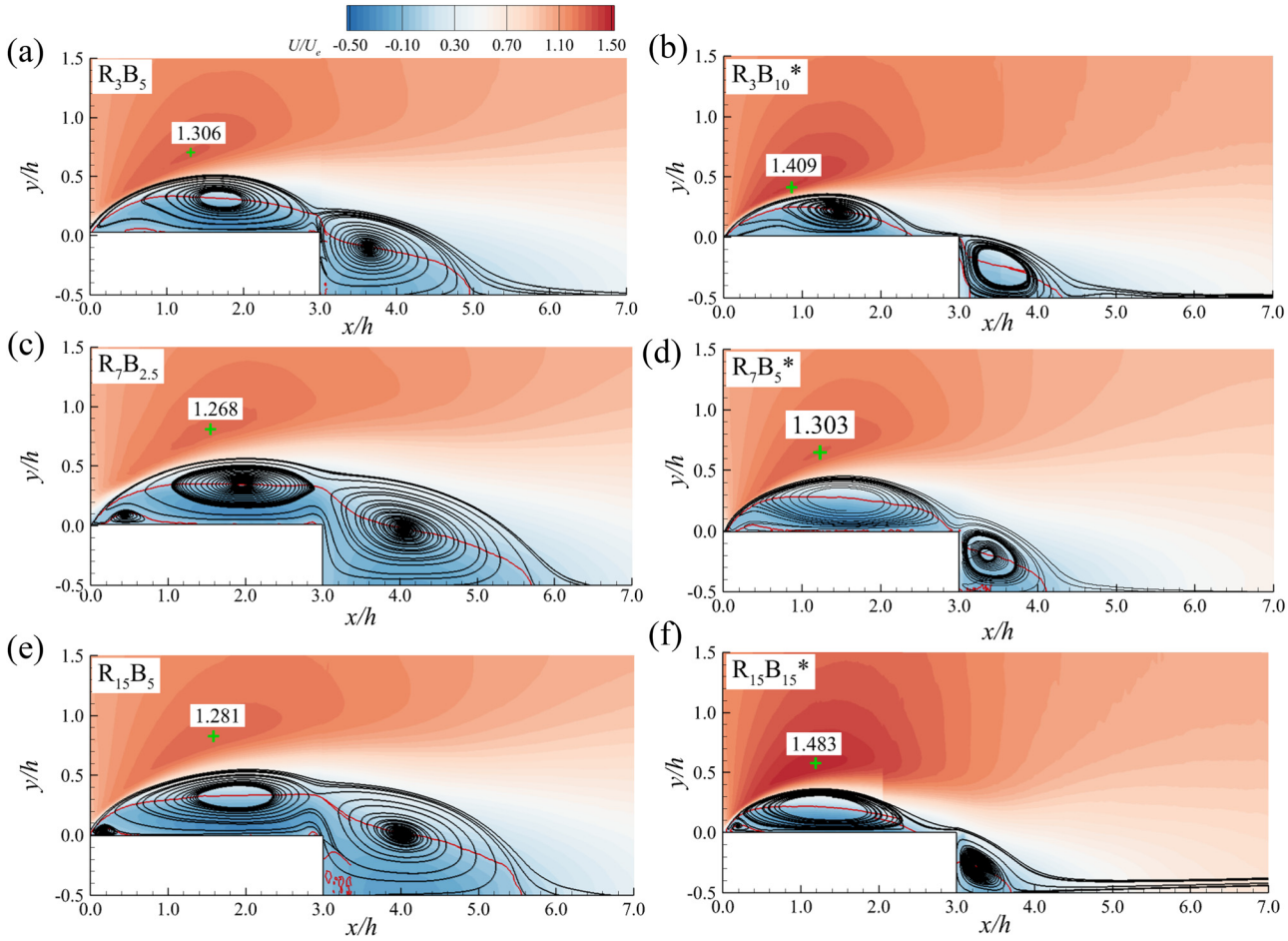


**FIG. 3.** Contours of streamwise mean velocity ($U$) superimposed with representative mean streamlines and the isopleth of $U = 0$ (red continuous line) for the test cases of (a) $R_3B_5$, (b) $R_3B_{10}$*, (c) $R_7B_{2.5}$, (d) $R_7B_5$*, (e) $R_{15}B_5$, and (f) $R_{15}B_{15}$*.

curvature of the separated shear layer increases due to more aggressive entrainment of the ambient fluid, and the tendency of mean flow reattachment onto the prism increases. Indeed, according to Nakagawa *et al.* (1999), increasing the blockage ratio constraints the vertical extent of the separated shear layer and facilitates an early flow reattachment. As shown in these figures, the primary and wake vortices decrease in size with a distinct separation between these vortices. Owing to the more intense flow reversal associated with the larger primary vortex for the unattached cases, the adverse pressure gradient is more intense leading to formation of larger and more distinct secondary vortex. The magnitude of the maximum velocity over the prism increases with blockage ratio. Moore *et al.* (2019b) and Liu *et al.* (2023) investigated the effects of Reynolds number on rectangular prisms. They showed that for the $d/h = 3$ prism, mean flow reattachment is strongly dependent on Reynolds number. However, the results shown in Fig. 3 clearly demonstrate that whether the mean flow reattaches onto the prism or not is not solely dictated by the Reynolds number but also the blockage ratio.

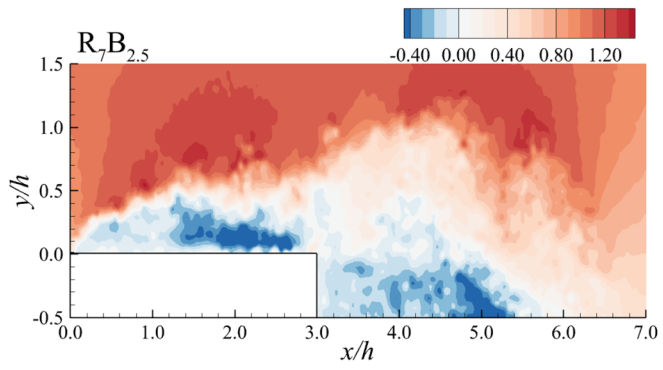


**FIG. 4.** A representative snapshot of instantaneous streamwise velocity for the $R_7B_{2.5}$ test case. Multimedia available online.

The present data and results from previous investigations at various blockage ratios and Reynolds numbers (Nakagawa *et al.*, 1999; Moore *et al.*, 2019b; Moore *et al.*, 2019b; and Liu *et al.*, 2023) are summarized in Fig. 5(a) to examine the effects of blockage ratio and Reynolds number on mean flow reattachment. It is interesting to see that the parametric space of $BR$ and Re can be classified into two

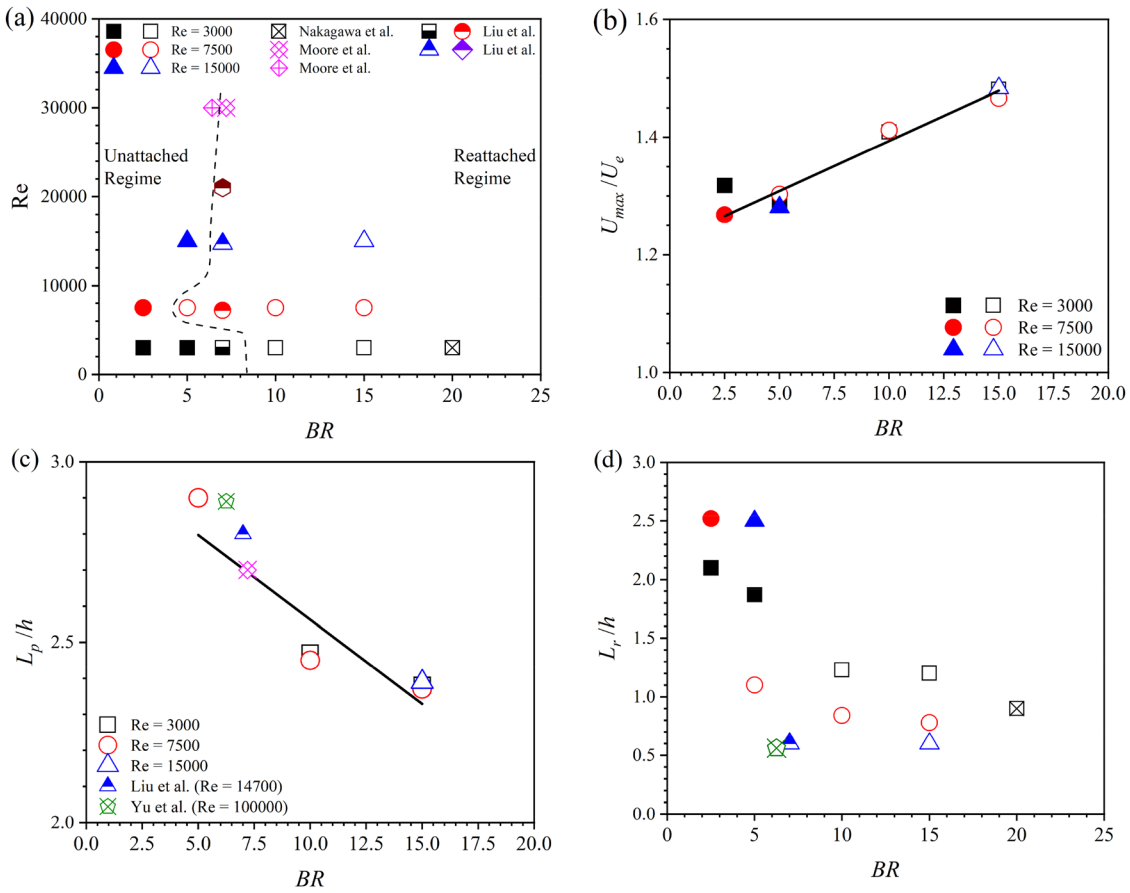


**FIG. 5.** (a) Classification of the different tested cases into the two regimes, namely unattached and reattached regimes. Variation of (b) $U_{max}/U_e$, (c) reattachment length over the prism ($L_p/h$), and (d) recirculation length ($L_r/h$) with blockage ratio for different Reynolds numbers. For clarity, solid symbols are used to represent the unattached test cases, while the corresponding open symbols indicate the reattached test cases for the present study. Data from Liu *et al.* (2023) are represented by semi-filled symbols.

regimes, namely unattached and reattached regimes, demarcated by a dashed line in Fig. 5(a). At lower blockage ratios and Reynolds numbers, the $d/h = 3$ falls into the unattached regime. However, as the blockage ratio and Reynolds number increase, the prism transits into the reattached regime. The critical blockage ratio can be viewed as the minimum blockage ratio at which the mean flow reattaches onto the surface of the prism for a specific Reynolds number. It is noted in Fig. 5(a) that the critical *BR* decreases as Reynolds number increases. This is expected as the probability of mean flow reattachment occurring increases at high Reynolds number (Okajima, 1982). For example, at Re = 3000, the critical blockage ratio is 10%, whereas the critical blockage ratio for Re = 7500 is at 5%.

The effects of blockage ratio and Reynolds number on separated flows can be quantified using such metrics as the maximum mean velocity, mean reattachment length over the prism, and recirculation length in the wake region. The isopleths of the zero mean velocity shown in Fig. 3 are used to identify the reattachment point onto the surface of the prisms, and the reattachment length ($L_p/h$) is defined as the streamwise distance from the leading edge to the point where the $U = 0$ line intersects with the top surface of the prism. Similarly, the recirculation length ($L_r/h$) is defined as the streamwise distance between the trailing edge and the intersection point of the zero mean velocity and the centerline. Figure 5(b) shows that the maximum velocity, $U_{max}/U_e$, is independent of Reynolds number but increases linearly with blockage ratio. This increase is attributed to the reduced area caused by the higher blockage, which in turn causes a stronger acceleration of the flow. The reattachment lengths for the various reattached test cases are shown in Fig. 5(c). Data from previous studies are included for the purpose of comparison. While the reattachment length is nearly independent of Reynolds number, it tends to decrease with increasing blockage ratio. For example, the reattachment length decreased by 16% when the blockage ratio is increased from 5% to 10%.

The effects of blockage ratio on the recirculation length are examined in Fig. 5(d). As blockage ratio increases, the recirculation length decreases monotonically. For example, $L_r/h$ for $R_3B_{15}{}^*$ is 1.2, which is only half of that for $R_3B_{2.5}$. The recirculation length is dictated by the occurrence or lack of mean flow reattachment. For the reattached test cases, a boundary layer develops briefly after the mean reattachment point, and a second separation occurs at the trailing edge to form the wake vortex. Conversely, the recirculation lengths of the unattached test cases are significantly longer. This is due to the large wake vortices

formed behind the prisms due to the intermittent detachment and reattachment of the separated shear layer.

### B. Reynolds normal stresses

The contours of the Reynolds normal stresses are presented to investigate the influence of blockage ratio and Reynolds number on the shear layers around the prisms. Figure 6 shows the contours of the streamwise Reynolds normal stress ($\overline{u'u'}$) superimposed with a mean streamline along the separated shear layer. Evidently, $\overline{u'u'}$ intensifies along the separated shear layer. The streamwise fluctuation possesses dual peaks along the shear layer over the prism and in the wake. In all test cases, the intensity of $\overline{u'u'}$ is higher over the prism compared to the wake region. In cases where mean reattachment occurs, the peak magnitudes are comparable. The locations of $\overline{u'u'}$ above the prism are closer to the leading edge for the reattached test cases compared to the unattached test cases. Meanwhile, the peak locations in the wake of the unattached test cases are further away from the trailing edge. Similar observations were made by Liu *et al.* (2023) and Kuroda *et al.* (2007) for the $d/h = 2$ prism. This difference in peak locations reflects the distinct flow dynamics between reattached and unattached cases, and thus underscores the importance of combined effects of blockage ratio and Reynolds number on the turbulent motions.

Contours of the normal Reynolds stress ($\overline{v'v'}$) shown in Fig. 7 also exhibit elevated regions over and in the wake region of the prism. However, in contrast to the streamwise fluctuations, the intensity of the normal fluctuations is notably higher in the wake compared to that over the prism. The enhanced region of normal fluctuations along the centerline is attributed to the formation of the von Kármán vortex street (Alves Portela *et al.*, 2017; Kumahor and Tachie, 2022). The strength of the normal fluctuations is significantly influenced by the blockage ratio and Reynolds number. For a given Reynolds number, increasing the blockage ratio increases the magnitude of $\overline{v'v'}$ (except at $\mathrm{Re} = 3000$). Also, for a given blockage ratio, the magnitude of $\overline{v'v'}$ increases with Reynolds number. Similar Reynolds number effects

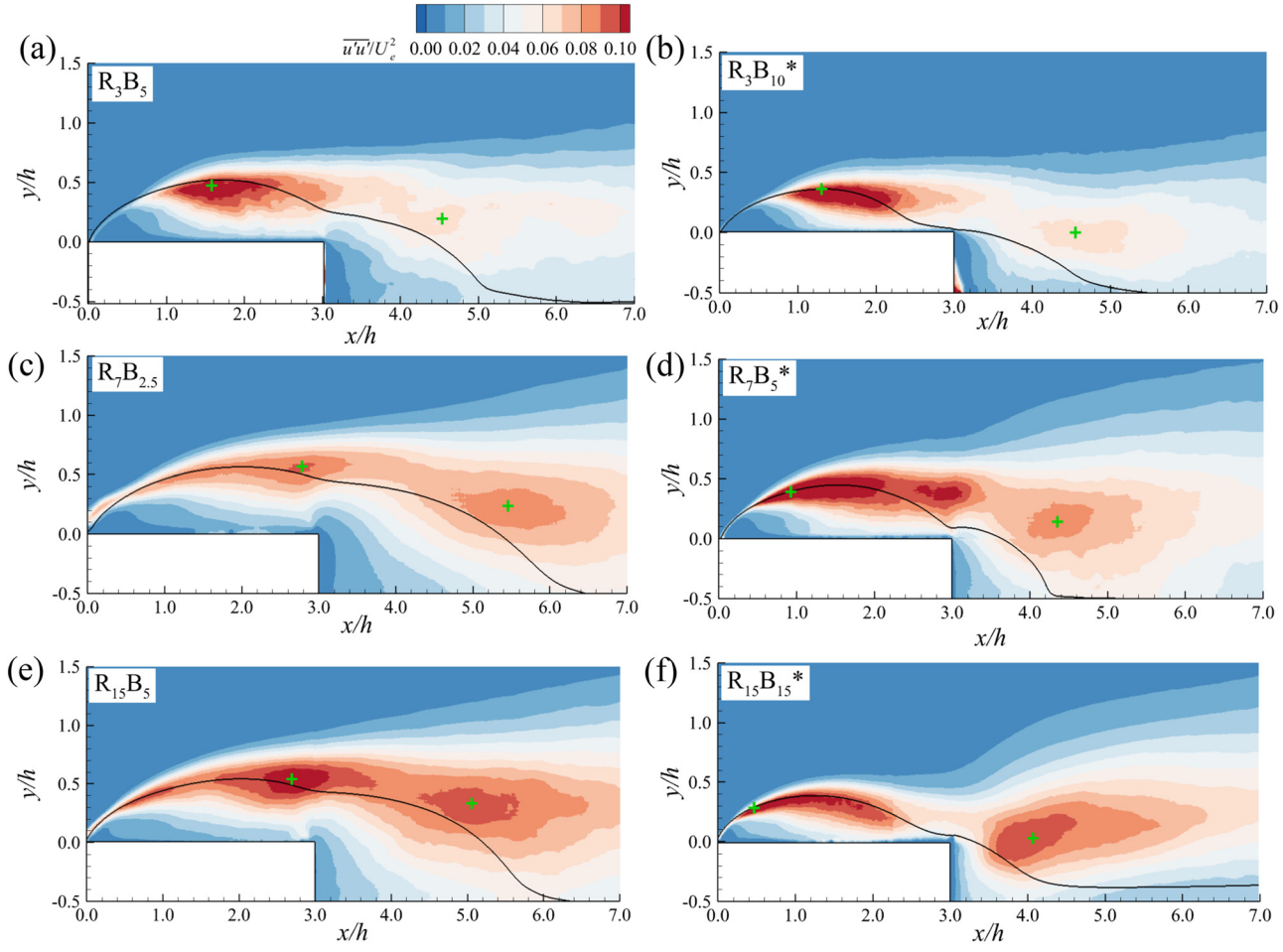


**FIG. 6.** Contours of streamwise Reynolds normal stress ($\overline{u'u'}$) superimposed with a mean streamline along the separated shear layer. for the test cases of (a) $R_3B_5$, (b) $R_3B_{10}^*$, (c) $R_7B_{2.5}$, (d) $R_7B_5^*$, (e) $R_{15}B_5$, and (f) $R_{15}B_{15}^*$. The "+" signs denote the peak locations.

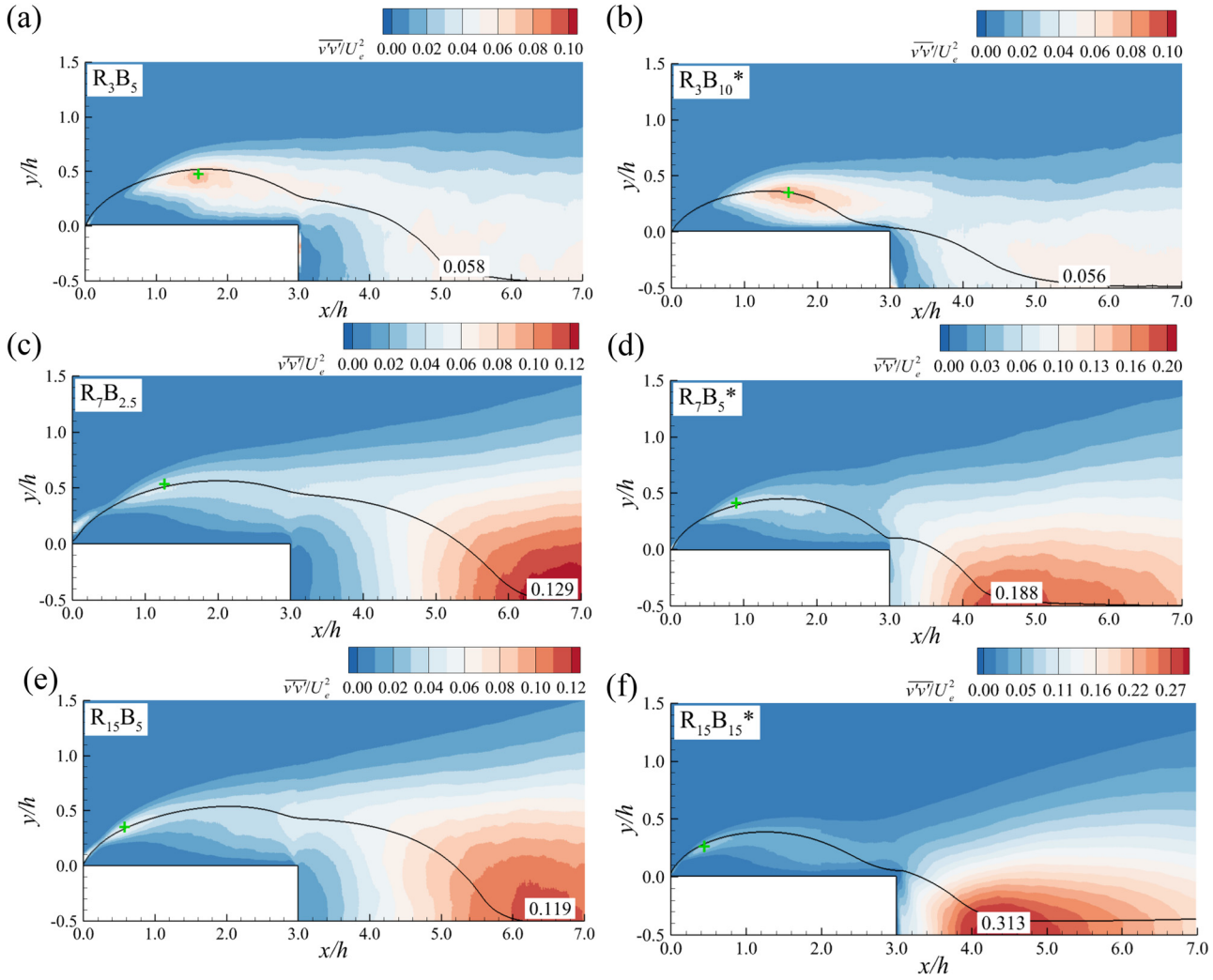


**FIG. 7.** Contours of normal Reynolds normal stress ($\overline{v'v'}$) superimposed with a mean streamline along the separated shear layer. for the test cases of (a) $R_3B_5$, (b) $R_3B_{10}^*$, (c) $R_7B_{2.5}$, (d) $R_7B_5^*$, (e) $R_{15}B_5$, and (f) $R_{15}B_{15}^*$.

were made by Liu *et al.* (2023) and Kumahor and Tachie (2023) for flow around rectangular cylinders in a uniform flow. It should be noted that the magnitude of $\overline{v'v'}$ for $R_7B_5^*$ is higher than $R_{15}B_5$, which can be attributed to the occurrence of flow reattachment right at the trailing edge in the former test case. The peak location of $\overline{v'v'}$ is closer to the trailing edge for the reattached test cases. This can be connected to the curvature of the shear layer and the reduction in the wake vortex formation. In the reattached test cases [see Figs. 3(b), 3(d), and 3(f)], a second separation occurs after the flow reattaches onto the face of the prism, and the shear layer rolls up to form vortices behind the prism. Meanwhile, the large recirculation region behind the prisms of the unattached test cases leads to weaker shedding of vortices, resulting in relatively low normal fluctuations in the near-wake region. According to Nakagawa *et al.* (1999), the presence of large recirculation region is associated with low normal fluctuations, which aligns with the observations made in the present study.

### C. Frequencies of the Kelvin–Helmholtz (KH) and von Kármán (VK) vortices

The effects of blockage ratio and Reynolds number on the dominant von Kármán shedding frequency are examined using frequency spectra. Figure 8 presents the spectra of the streamwise and normal velocity fluctuations at the location of maximum $\overline{u'u'}$ over the prism and maximum $\overline{v'v'}$ in the wake, respectively. For this, the Welch's overlapped window techniques (Welch, 1967) was implemented to calculate the frequency spectra. The window size of the Fourier transformation was 5000 snapshots (which corresponds to 6.3 s), and the overlap between adjacent windows was 15 snapshots (which corresponds to 0.02 s). As seen in the right column in Fig. 8, for the reattached test cases ($R_3B_{10}^*$, $R_7B_{10}^*$, and $R_{15}B_{15}^*$), the spectra of both $\phi_{uu}$ and $\phi_{vv}$ reveal a single distinct peak reflecting the von Kármán shedding frequency. Specifically, the Strouhal numbers for the cases of $R_3B_{10}^*$, $R_7B_{10}^*$, and $R_{15}B_{15}^*$ are 0.171, 0.164, and 0.173, respectively. It

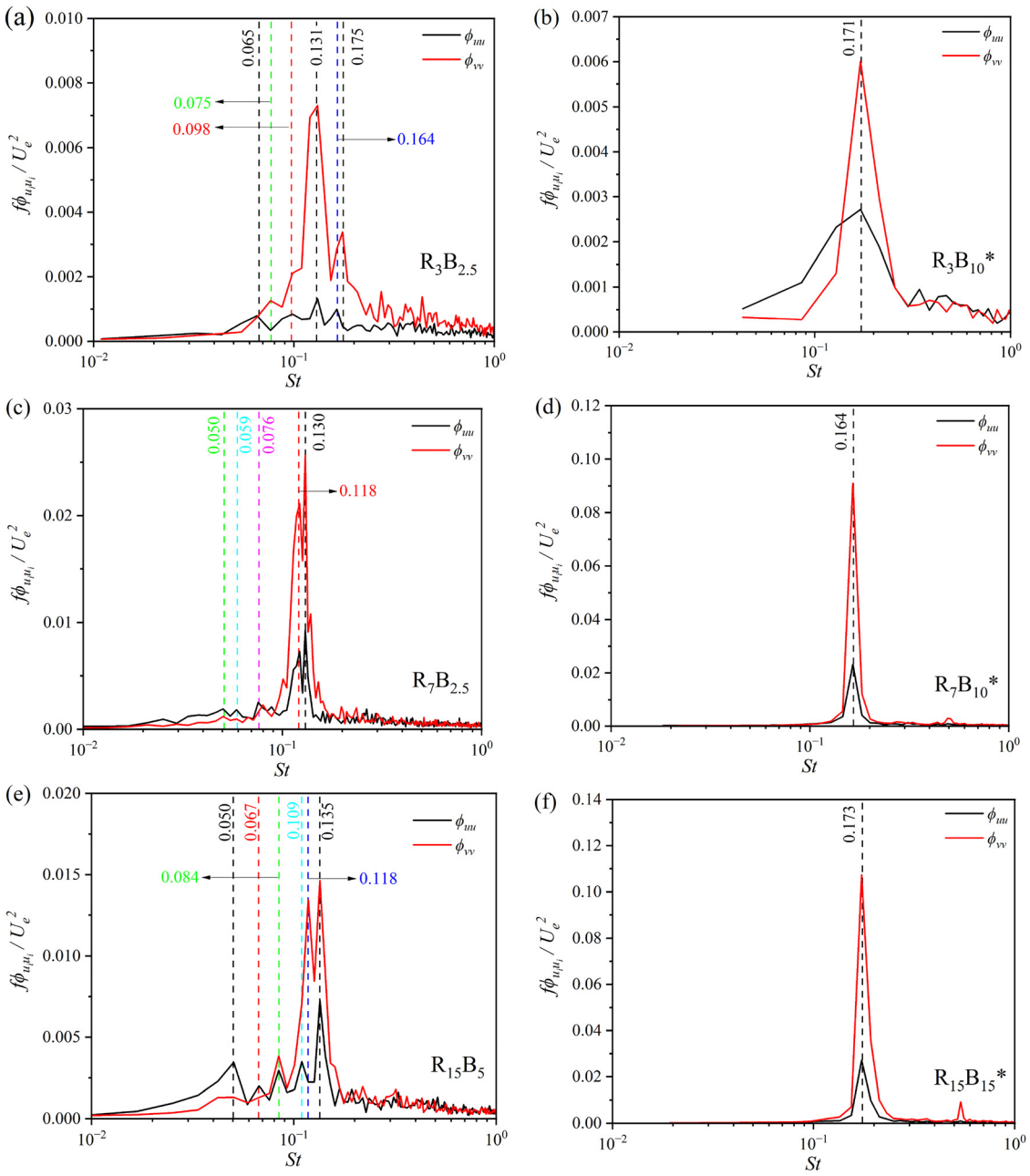


**FIG. 8.** Frequency spectra of the velocity fluctuations ($\phi_{u_iu_i}$) at the location of maximum $\overline{u'u'}$ and $\overline{v'v'}$ for the test cases of (a) $R_3B_{2.5}$, (b) $R_3B_{10}^*$, (c) $R_7B_{2.5}$, (d) $R_7B_{10}^*$, (e) $R_{15}B_5$, and (f) $R_{15}B_{15}^*$.

is noted that the peak magnitude based on $v'$ for $R_3B_{10}^*$ [Fig. 8(b)] is an order of magnitude lower than the other reattached cases due to the weak fluctuations and vortex shedding as concluded from Fig. 7(b). However, in Figs. 8(a), 8(c), and 8(f), where mean flow does not reattach on the prism, multiple peaks are observed. This is attributed to the interaction of the shear layers over the prism and in the near-wake region as well as the intermittent reattachment and detachment of the separated shear layer. The observation of single and multiple Strouhal numbers for the reattached and unattached test cases, respectively, are in good agreement with the previous studies of Okajima (1982), Igarashi (1985), and Norberg (1993). The von Kármán shedding frequencies for all test cases along with existing data in the literature are shown in Fig. 9. The dominant frequencies are also consistent with previous studies. For instance, for

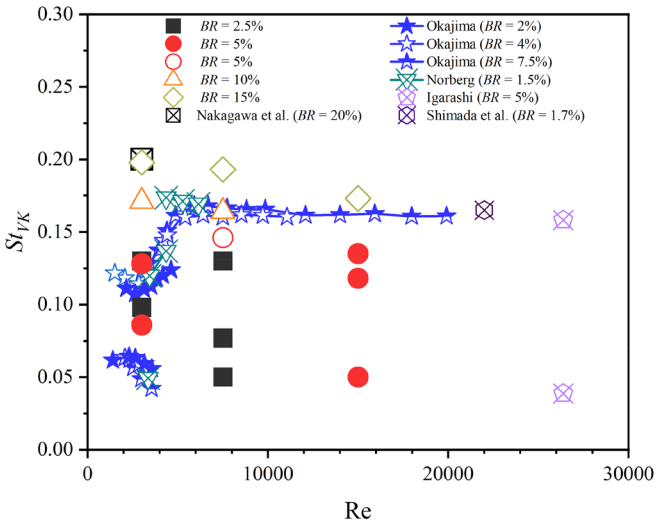


**FIG. 9.** Variation of $St_{VK}$ with Reynolds number and blockage ratio. Data from previous studies are included.

Re = 3000, $St = 0.198$ at $BR = 15\%$ compared to 0.20 reported by Nakagawa *et al.* (1999) at $BR = 20\%$.

While the von Kármán shedding frequency can be detected everywhere around the prism, the KH vortices, being a convective instability, can only be detected over a short distance downstream of its origin (Moore *et al.*, 2019a). To detect the KH frequencies, selected locations along the shear layer were probed, and the frequency spectra of the streamwise fluctuations are presented in Fig. 10. The KH instability appears as a broadband peak at a relatively higher frequency compared to the von Kármán. The dominant frequency associated with the von Kármán shedding in the near-wake region can be seen everywhere along the shear layer except at Re = 3000, which is due to the weak velocity fluctuation at Re = 3000 [see Figs. 7(a) and 7(b)]. Close to the leading edge, a broadband peak is observed at a high frequency. The peak broadens and becomes prominent further downstream of the leading edge. Along the shear layer, additional peaks are observed, which coincide with the subharmonics of the KH frequency. The appearance of the subharmonics is due to the vortex pairing mechanism (Brun *et al.*, 2008; Moore *et al.*, 2019a; and Fang *et al.*, 2022). As the small-scale vortices are convected downstream, they merge to form a single vortex at half the frequency. For instance, in Fig. 10(a), at $x/h = 0.20$, a single broadband peak is observed at $St = 1.615$, which coincides with the KH frequency. Further downstream at $x/h = 0.45$, another peak emerges at half the KH frequency ($St = 0.807$), indicating the vortex pairing mechanism.

The KH frequency and the ratio of KH to VK frequency are presented in Fig. 11. For clarity, the filled and hollow symbols are for the unattached and reattached test cases, respectively. As shown in Fig. 11(a), the frequency associated with the KH instability increases with blockage ratio for a given Reynolds number. The presence of the KH instability indicates the onset of transition from laminar to turbulent regime in the separated shear layer. As blockage ratio and Reynolds number increase, the location of the first peak is detected closer to the leading edge indicating early transition from laminar to turbulence. Reynolds number effect is consistent with earlier studies that transition occurs sooner, and the KH frequency increases with Re (Lander *et al.*, 2018; Moore *et al.*, 2019a). Since blockage ratio also promotes an earlier transition and increases the Strouhal number, it has a similar effect as the Reynolds number. The frequency ratio presented in Fig. 11(b) shows more significant Reynolds number effect for the reattached test cases compared to the unattached test cases. For instance, $St_{KH}/St_{VK}$ is 12.7 and 18.7 for $R_3B_5$ and $R_{15}B_5$, respectively, compared to 12.7 and 44.9 for $R_3B_{15}{}^*$ and $R_{15}B_{15}{}^*$, respectively.

### D. Two-point correlation and integral time scale

The effects of blockage ratio and Reynolds number on the spatial coherency of the large-scale structures and the interactions between the shear layer over and in the wake of the prism are further examined using the two-point autocorrelation function, which is defined as follows:

$$R_{u_iu_j} = \frac{\overline{u_i'(\boldsymbol{X}_{ref})u_j'(\boldsymbol{X}_{ref} + \Delta\boldsymbol{X})}}{u_{i,\,rms}'(\boldsymbol{X}_{ref})u_{j,\,rms}'(\boldsymbol{X}_{ref} + \Delta\boldsymbol{X})}. \tag{2}$$

Here, $\boldsymbol{X}_{ref}$ represents the reference position, and $\Delta\boldsymbol{X}$ is a spatial displacement. Figure 11 presents contours of the autocorrelation of the streamwise velocity fluctuations ($R_{uu}$) with the reference point at $0.1h$ above the trailing edge of the prisms for test cases $R_3B_{2.5}$, $R_3B_{10}{}^*$, $R_7B_{2.5}$, $R_7B_{10}{}^*$, $R_{15}B_5$, and $R_{15}B_{15}{}^*$. This reference point is chosen to sensitize the vortical structures passing over the trailing edge and potential interaction of the separation bubble over and behind the prisms. The vectors of $R_{uu}$, $R_{uv}$ provide an estimation of the dominant spanwise vortical structures based on the streamwise fluctuation at the reference position (Kevin *et al.*, 2019). It is seen that the spatial coherence of the vortical structures is significantly influenced by both blockage ratio and Reynolds number. From Figs. 12(a), 12(c), and 12(e), the structures are correlated over a large distance. This is indicative of a strong influence of the wake on the separated shear layer emanating from the leading edge of the prism. For the reattached test cases [Figs. 12(b), 12(d), and 12(f)], on the other hand, the values of the autocorrelation decay quickly, which indicates the independence of the separation bubbles. With an increase in blockage ratio and Reynolds number, the decay rate increases. Although not shown here, a similar pattern is also observed from the autocorrelation of $R_{vv}$. The rate of decay can be associated with the point of reattachment on the face of the prism. When mean flow reattachment occurs closer to the leading edge, there is a sufficient separation between the bubbles over and behind the prism. This provides a greater level of independence between the separation bubbles, leading to a faster decorrelation of the structures. For instance, comparing $R_7B_{10}{}^*$ [Fig. 12(d)] and $R_{15}B_{15}{}^*$ [Fig.12(f)], the rate of decay is faster in the latter since the reattachment point was closer to the leading edge of the body.

Kiya and Sasaki (1983) used the integral time scales to analyze the time scales along the separation bubble formed along the sides of a blunt flat plate. More recently, Moore *et al.* (2019a) analyzed the time scales of rectangular prisms at selected locations using hot-wire anemometry. The present study takes advantage of the availability of whole-field time-resolved data to analyze the integral time scale over the entire flow field including the recirculation region. The integration was performed over the range of time displacement from zero to the first zero crossing of the temporal autocorrelation function of $R_{uu}$. Figure 13 presents the contours of the integral time scales ($\tau$) to

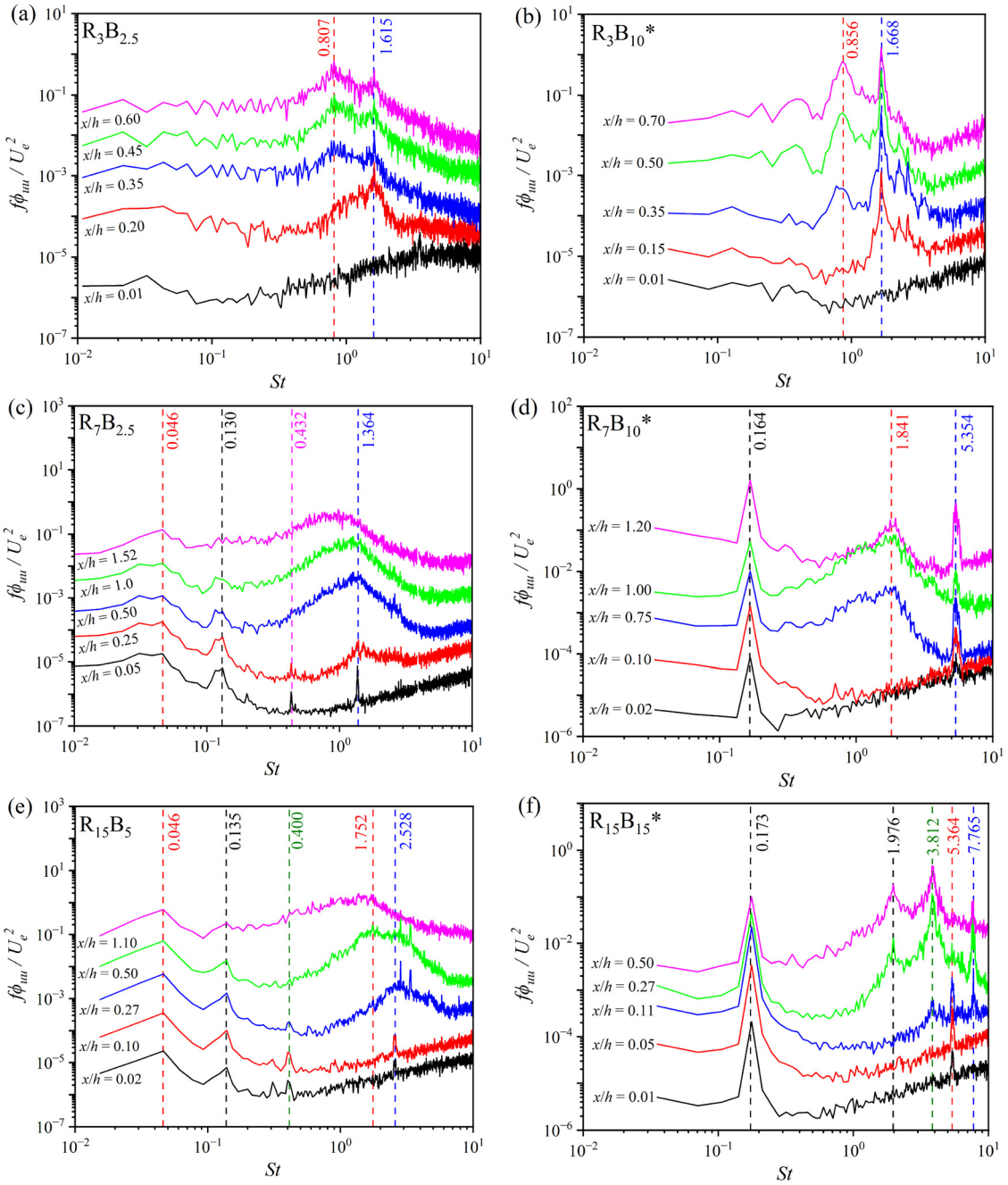


**FIG. 10.** Frequency spectra of the streamwise fluctuating velocities along the shear layer for the test cases of (a) $R_3B_{2.5}$, (b) $R_3B_{10}{}^*$, (c) $R_7B_{2.5}$, (d) $R_7B_{10}{}^*$, (e) $R_{15}B_5$, and (f) $R_{15}B_{15}{}^*$. To facilitate visualization, each location is vertically offset.

highlight the differences between the flow dynamics of the two regimes. For the reattached test cases [Figs. 13(b), 13(d), and 13(f)], a small region of elevated integral time scale is located within the separation bubble very close to the leading edge of the prisms, whereas elevated region of integral time scale is observed over a wide range for the unattached tests cases [Figs. 13(a), 13(c), and 13(e)]. This region is more prominent compared to the reattached test cases. The presence of these elevated integral scales is reminiscent of low-frequency flapping motion of the reverse flow region (Kiya and Sasaki, 1983; Fang *et al.*, 2022). Similar observation was made by Moore *et al.* (2019a) for a square (short regime) and a $d/h = 5$ (long regime) prisms. They attributed the difference in the time scales to mean flow reattachment, which is evident from the plots in

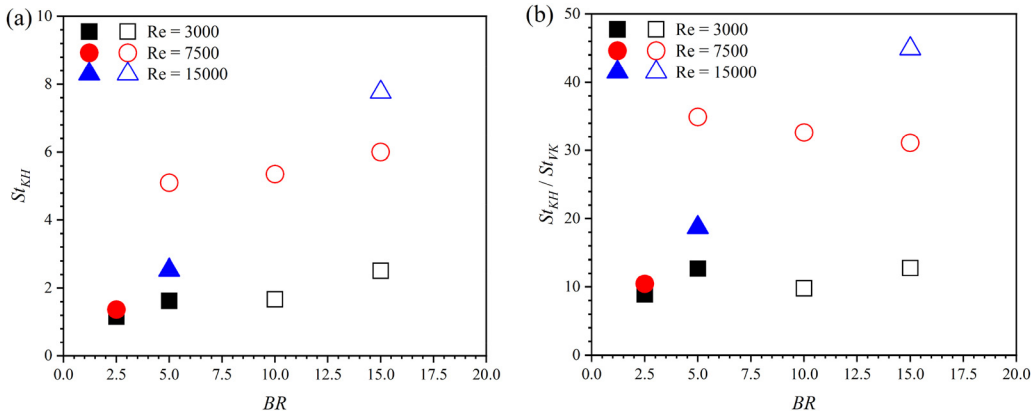


**FIG. 11.** (a) Variation of $St_{KH}$ and (b) variation of $St_{KH} / St_{VK}$ with blockage ratio.

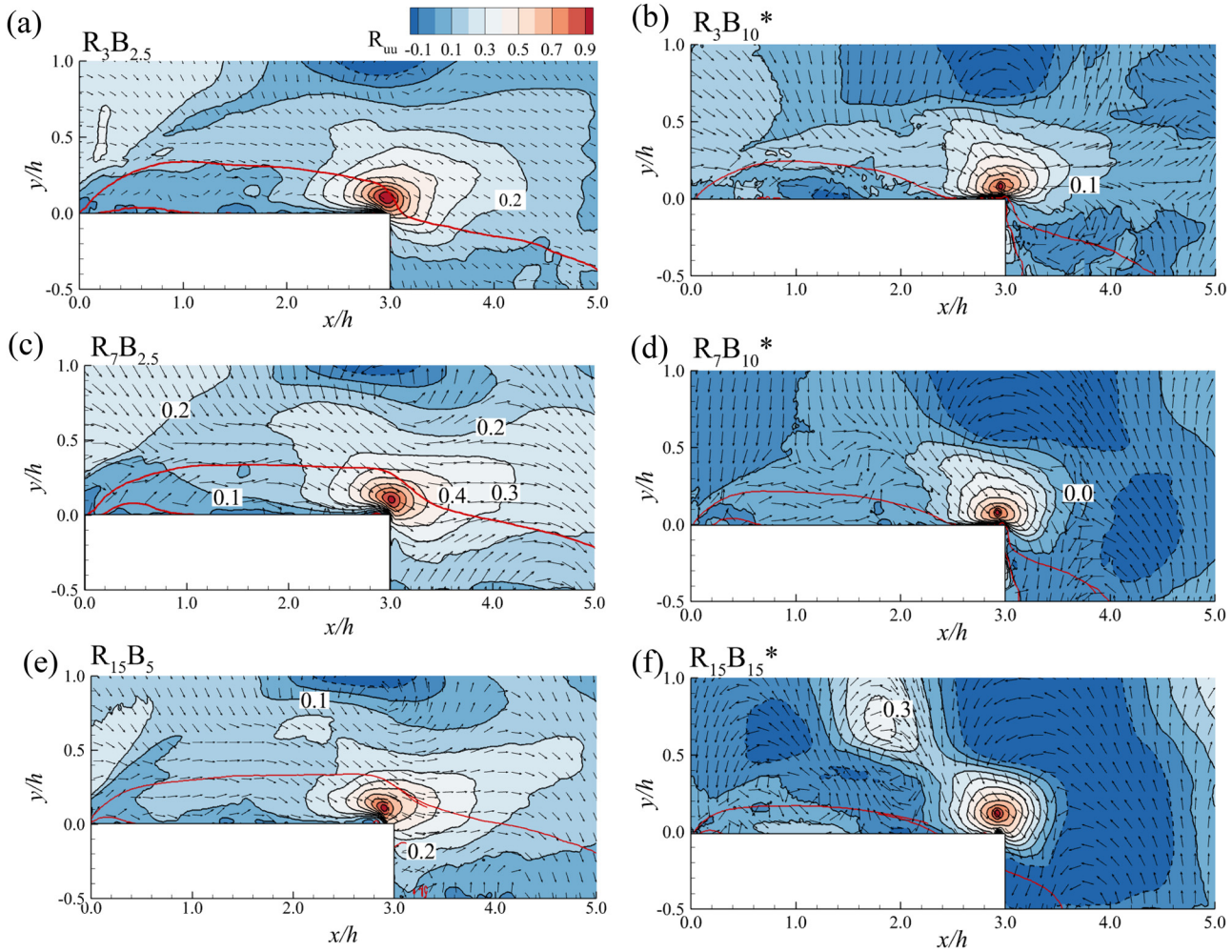


**FIG. 12.** Contours of $R_{uu}$ at $0.1h$ above the trailing edge of the prism for (a) $R_3B_{2.5}$, (b) $R_3B_{10}{}^*$, (c) $R_7B_{2.5}$, (d) $R_7B_{10}{}^*$, (e) $R_{15}B_5$, and (f) $R_{15}B_{15}{}^*$. Contour levels are at intervals of 0.1 and from −0.1 to 0.9. The red continuous line is the isopleth of $U = 0$.

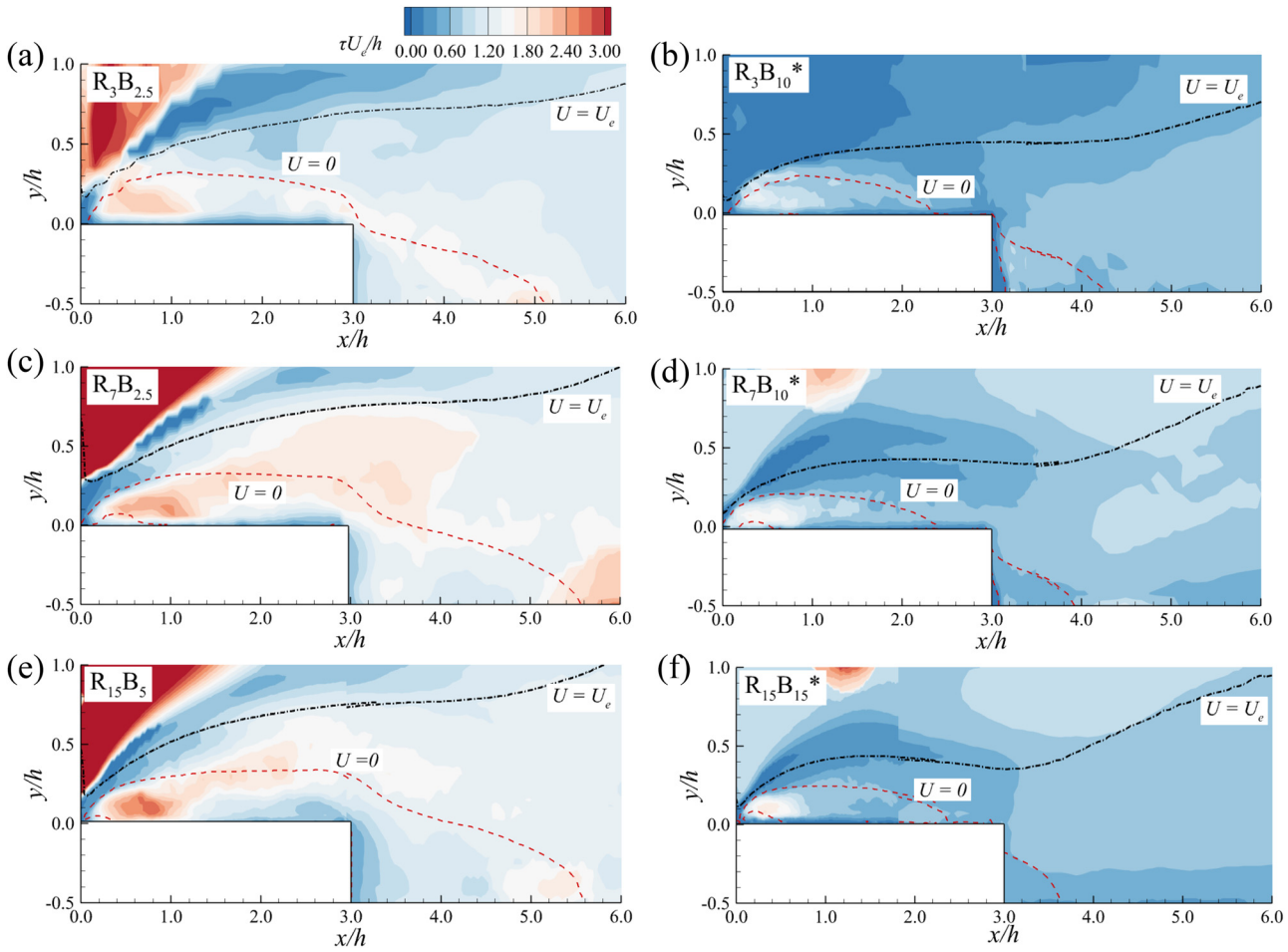


**FIG. 13.** Contour of the integral time scales ($\tau$). The red and black continuous lines are the isopleths of $U = 0$ and $U = U_e$, respectively. (a) $R_3B_{2.5}$, (b) $R_3B_{10}^*$, (c) $R_7B_{2.5}$, (d) $R_7B_{10}^*$, (e) $R_{15}B_5$, and (f) $R_{15}B_{15}^*$.

the present study. These results further show the dynamic coupling between the two separation bubbles for the unattached test cases.

### E. Proper Orthogonal Decomposition (POD)

Proper orthogonal decomposition (POD) was performed to further elucidate the effects of blockage ratio and Reynolds number on the dynamic roles of vortical structures and their relative contribution to the vortex shedding process. In the present study, the snapshot method originally proposed by Sirovich (1987) along with the detailed procedures and implementation provided by Riches *et al.* (2018), Fang and Tachie (2019), and Nguyen *et al.* (2020) was employed. The fluctuating velocity fields $[u_i'(x, y, t)]$ were decomposed into a set of spatial eigenfunctions (modes) $(\Psi^k)$ multiplied by their associated temporal mode coefficient $a^k(t)$ as

$$u_i'(x, y, t) = \sum_{k=1}^{M} \Psi_i^k(x, y) a^k(t), \tag{3}$$

where $M$ is the number of modes. For each test case, the POD analysis was conducted over the entire field of view of both cameras excluding the area covered by the prism. As outlined by Riches *et al.* (2018) among others, two POD modes typically pair up to represent a coherent motion such as the von Kármán vortex shedding motion in the wake. These mode pairs must have identical energy content, their temporal coefficient must be phase shifted by 90° and the quasi-periodical spatial modes must be shifted by one-quarter wavelength of the coherent structures.

The relative contribution of the streamwise and normal velocity fluctuations to the turbulent kinetic energy by the first four modes are shown in Figs. 14(a)–14(c), while Fig. 14(d) presents the fractional energy distribution of the first 10 POD modes. As remarked by Nakagawa *et al.* (1999), Alves Portela *et al.* (2017), and Riches *et al.* (2018), for circular and rectangular prisms in a uniform flow, the von Kármán shedding motions are dominated by the normal velocity fluctuations. This is evident from the higher energy contribution by $v'$ for the first two POD modes for all test cases. For instance, for $R_{15}B_{15}^*$, $v'$ contributes about 76% and 70%, respectively, to the total energy content of modes 1 and 2. The energy content of the first two modes for the reattached test cases is significantly higher than the unattached test cases. At Re = 15 000, the combined energy from the first two modes

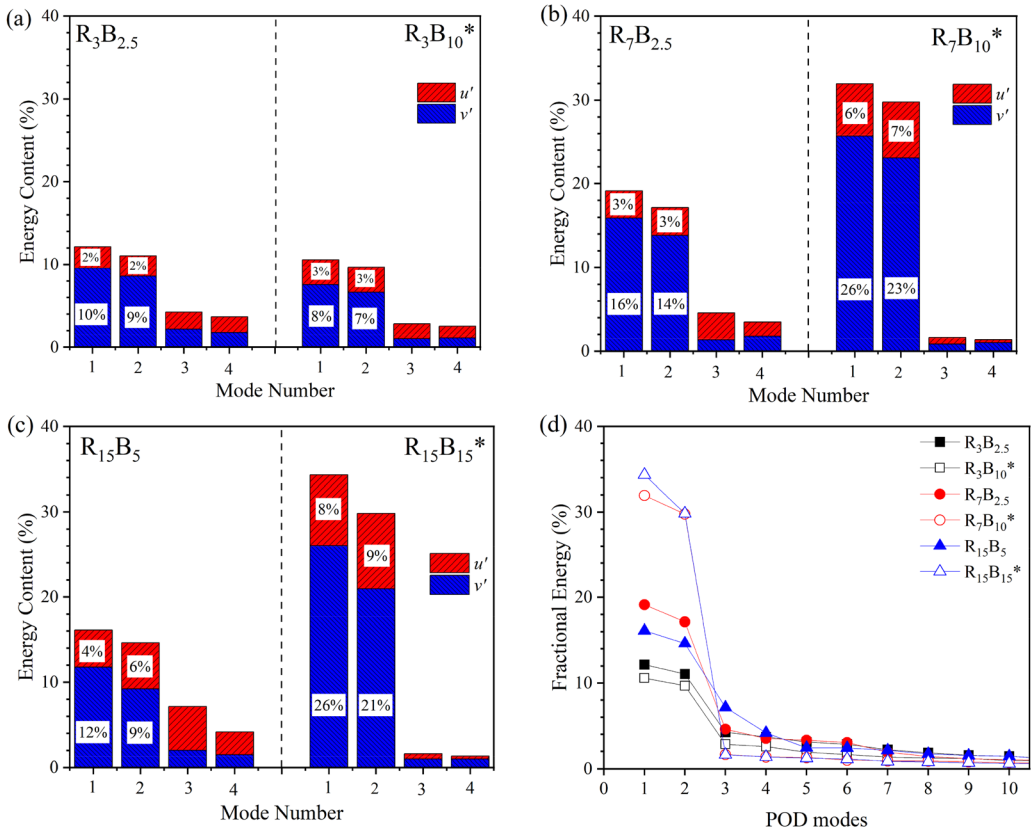


**FIG. 14.** (a)–(c) Relative contribution of the streamwise and normal velocity fluctuations to the turbulent kinetic energy by the first four modes and (d) fractional energy distribution of the first 10 POD modes.

is 64% at $BR = 15\%$ compared to 31% at $BR = 5\%$. It is noted that although mean flow reattachment occurred for $R_3B_{10}$*, the energy contents of the first two modes are relatively low. This is attributed to the weaker vortex shedding since the first two modes are associated with the large-scale vortices. Figure 14(d) also shows that the first two modes contain the highest and comparable energy content followed by a drastic energy reduction for the subsequent modes. For example, the energy contents of the first and second modes for $R_7B_{10}$* are 32% and 30%, respectively, but the combined energy content for modes 3–10 is 8%. Blockage ratio and Reynolds number have no significant effect on the energy content of the higher modes [Fig. 14(d)].

The first two spatial POD modes obtained from the normal velocity fluctuations for $R_7B_{2.5}$ and $R_7B_{10}$* are presented in Fig. 15 to analyze the spatial dynamics of the coherent structures. The superimposed vectors of $\Psi_u$ and $\Psi_v$ highlight the vortical structures. Both POD modes exhibit a train of alternating positive and negative structures behind the prisms, which are representative of the vortex shedding motion behind prisms in uniform flows. Additionally, the symmetrical nature of the von Kármán vortices is evident from the centerline location of the vortex cores, denoted by the "+" symbol. For each test case, the contours of the first and second POD are similar, except for a streamwise shift of one-quarter of wavelength of the vortical structures. The wavelength ($\lambda$) is defined as the streamwise distance between peak locations of structures with equal signs, and half wavelength ($\lambda/2$) is the distance between adjacent structures with opposite signs. Previous studies (Riches *et al.* 2018; Kumahor and Tachie, 2023) estimated the convective velocity of the large-scale structures using the wavelength and fundamental von Kármán shedding frequency as follows: $U_c/U_e = St_{VK} \times \lambda/h$. Table III summarizes the one-half wavelengths together with the corresponding convective velocities for all test cases. The convective velocities for the reattached test cases are $U_c/U_e = 0.81 \pm 0.06$. These values are consistent with $U_c/U_e = 0.83$ reported by Nakagawa *et al.* (1999) for the reattached case of the $d/h = 3$ prism who used movement of the vorticity peaks to determine the convective velocity. For the unattached test cases, the convective velocities are within values of $0.62 \pm 0.03$, which are 25% lower compared to the reattached cases.

Figure 16 presents the temporal variation of the first four POD mode coefficients and the respective phase portraits of the first two modes are shown in Fig. 17 for the six selected test cases. Regardless of blockage ratio or Reynolds number, the time signals of the first two modes exhibit sinusoidal patterns, and there is a phase shift between the two modes. The corresponding phase portraits of the first two

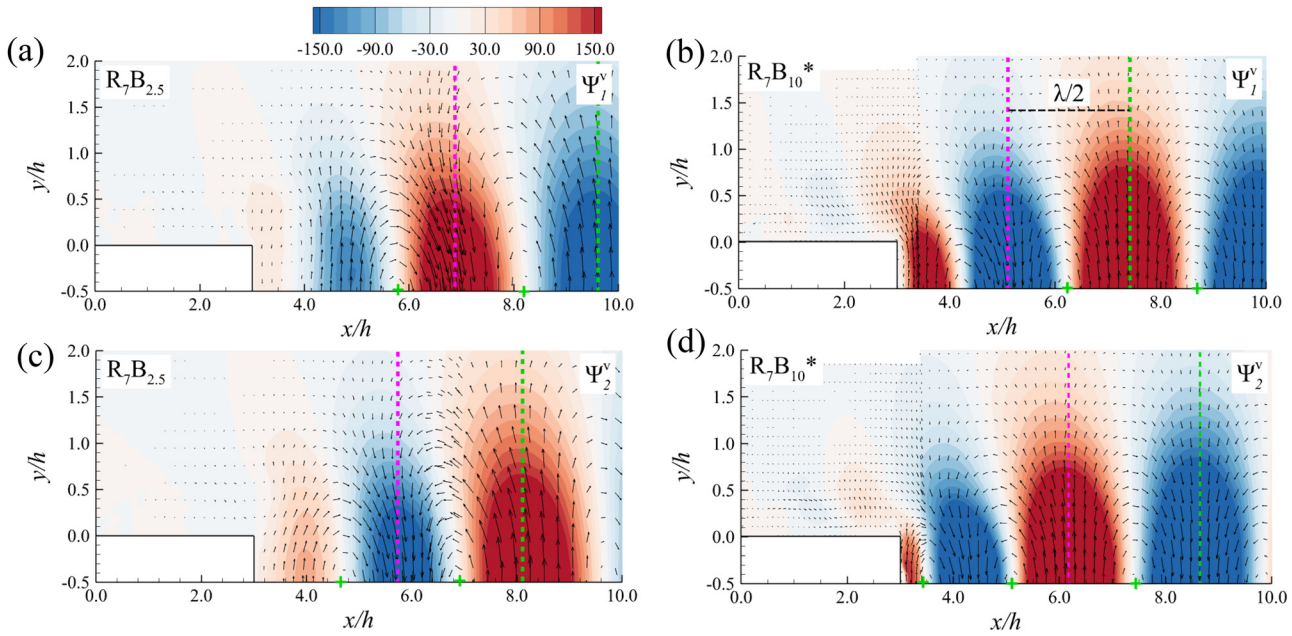


**FIG. 15.** Contour of modes 1 and 2 from the normal velocity fluctuations. (a) Mode 1 for $R_7B_{2.5}$, (b) mode 1 for $R_7B_{10}^*$, (a) mode 2 for $R_7B_{2.5}$, and (b) mode 2 for $R_7B_{10}^*$, (c) Mode 2 for $R_7B_{2.5}$, and (d) Mode 2 for $R_7B_{10}^*$.

POD modes also reveal a circular pattern. However, the time signals for $R_7B_{10}^*$ and $R_{15}B_{15}^*$ show similar amplitudes and the phase portraits reveal distinct circular orbits. This suggests that for the reattached test cases, the coherent structures are significantly more organized. On the other hand, the sinusoidal waves of $R_3B_{2.5}$, $R_7B_{2.5}$, and $R_{15}B_5$ show significant amplitude modulation, and the circular orbits are less distinct. This observation for the unattached test cases is attributed to the intermittent reattachment of the separated shear layer onto the prism. Similar observation was made by Kumahor and Tachie (2023) for the $d/h = 2$ prism where the flow did not reattach. Even though $R_3B_{10}^*$ is in the reattached regime, the time signal also exhibits amplitude modulation due to the low turbulence level and weak vortex shedding. These results further show that mean flow reattachment significantly modifies the vortical structures behind the prisms. Meanwhile, the time histories of $a^{(3)}$ and $a^{(4)}$ show no phase shift between them for all test cases, suggesting that the third and fourth modes are not mode pairs.

**TABLE III.** Summary of the one-half wavelengths, $St_{VK}$, and convective velocities.

| Test Case | $\lambda/2h$ | $St_{VK}$ | $U_c/U_e$ |
|---|---|---|---|
| $R_3B_{2.5}$ | 2.4 | 0.130 | 0.62 |
| $R_3B_5$ | 2.4 | 0.128 | 0.61 |
| $R_3B_{10}^*$ | 2.4 | 0.171 | 0.82 |
| $R_3B_{15}^*$ | 2.2 | 0.198 | 0.87 |
| $R_7B_{2.5}$ | 2.5 | 0.130 | 0.65 |
| $R_7B_5^*$ | 2.2 | 0.146 | 0.64 |
| $R_7B_{10}^*$ | 2.4 | 0.164 | 0.79 |
| $R_7B_{15}^*$ | 2.2 | 0.193 | 0.85 |
| $R_{15}B_5$ | 2.2 | 0.135 | 0.59 |
| $R_{15}B_{15}^*$ | 2.2 | 0.173 | 0.76 |

Figure 18 presents the frequency spectra of the temporal coefficient of modes 1 and 3. It should be noted that the spectra of modes 1 and 2 are similar; hence, only mode 1 is shown for conciseness. The spectra of the first POD modes possess dominant peaks at the fundamental shedding frequencies. These results indicate that the first mode pairs are indeed associated with the large-scale vortices. Meanwhile the spectra of the third POD mode show multiple peaks at lower and higher frequencies. For $R_7B_{10}^*$, the spectra of the third POD mode possess a peak at $St = 0.328$, which is a harmonic of the fundamental shedding frequency. For $R_3B_{2.5}$, $R_7B_{2.5}$, and $R_{15}B_5$ (unattached test cases), the peaks are observed at lower frequencies. It is noteworthy that the dominant peaks observed using the temporal POD mode coefficients are consistent with those obtained using the velocity fluctuations. Similar observations were made by Aleyasin *et al.* (2021) and Sagharichi *et al.* (2023).

## IV. SUMMARY AND CONCLUSION

The influence of blockage ratio ($BR$) and Reynolds number (Re) on the turbulent flow dynamics around rectangular prisms in a uniform flow is examined using time-resolved particle image velocimetry. The depth-to-thickness ratio of the prism ($d/h = 3$) was chosen as it falls within the intermediate regime where the flow dynamics are very sensitive to the incoming flow condition. The examined Reynolds numbers based on the prism thicknesses were 3000, 7500, and 15 000,

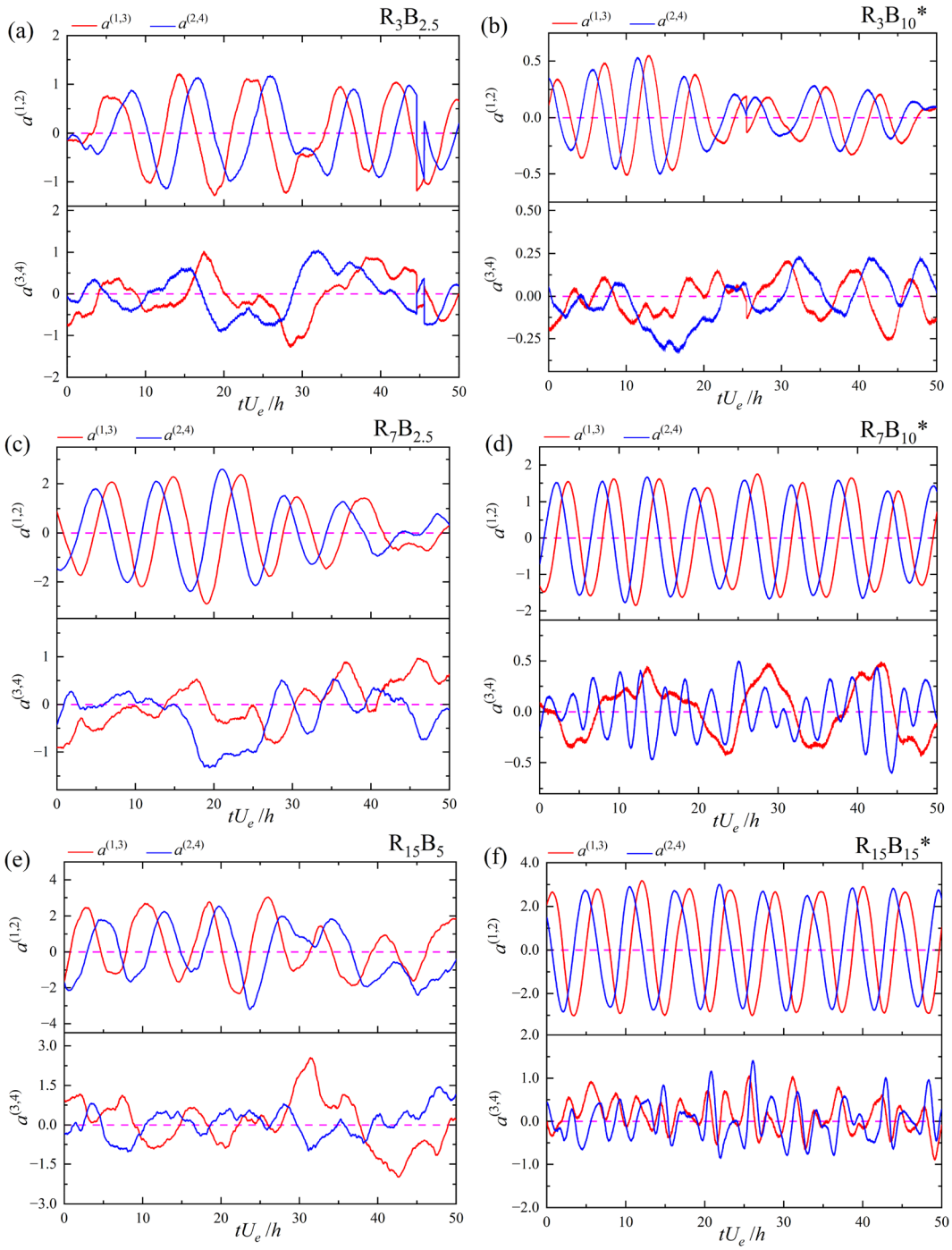


**FIG. 16.** Time signal of the first four modes. (a) $R_3B_{2.5}$, (b) $R_3B_{10}^*$, (c) $R_7B_{2.5}$, (d) $R_7B_{10}^*$, (e) $R_{15}B_5$, and (f) $R_{15}B_{15}^*$.

and the tested blockage ratios were 2.5%, 5%, 10%, and 15%. The results are discussed in terms of mean flow, Reynolds stress, frequency spectra, integral time scale, two-point correlation, as well as proper orthogonal decomposition (POD).

The mean flow possesses distinct recirculation bubbles over and behind the prisms. Two regimes are identified based on the mean flow characteristics. At low Re and *BR*, mean flow reattachment onto the surface of the prism is absent, and a large wake vortex forms behind

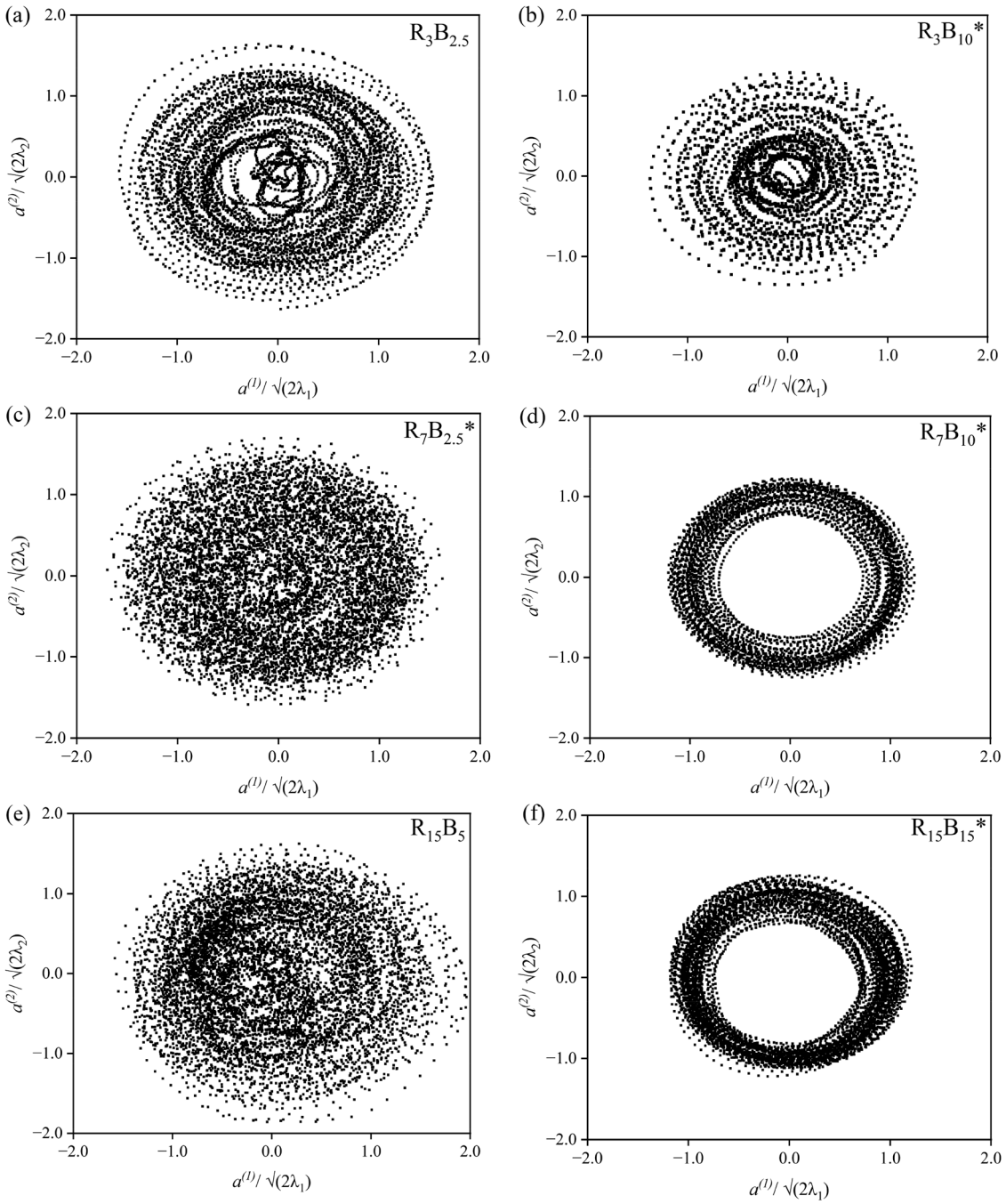


**FIG. 17.** Phase portraits of modes 1 and 2 for the test cases of (a) $R_3B_{2.5}$, (b) $R_3B_{10}^*$, (c) $R_7B_{2.5}$, (d) $R_7B_{10}^*$, (e) $R_{15}B_5$, and (f) $R_{15}B_{15}^*$.

the prism. However, when *BR* and Re increase, the separated mean flow reattaches onto the surface of the prism and a relatively small wake vortex is formed behind the prism. As blockage ratio increases, the maximum velocity over the prism also increases due to the reduced area. Contours of the Reynolds stresses show two peaks over and in the wake of the prisms. Relatively low normal fluctuations are observed in the near-wake region as a result of the large recirculation region behind the prisms for the unattached test cases.

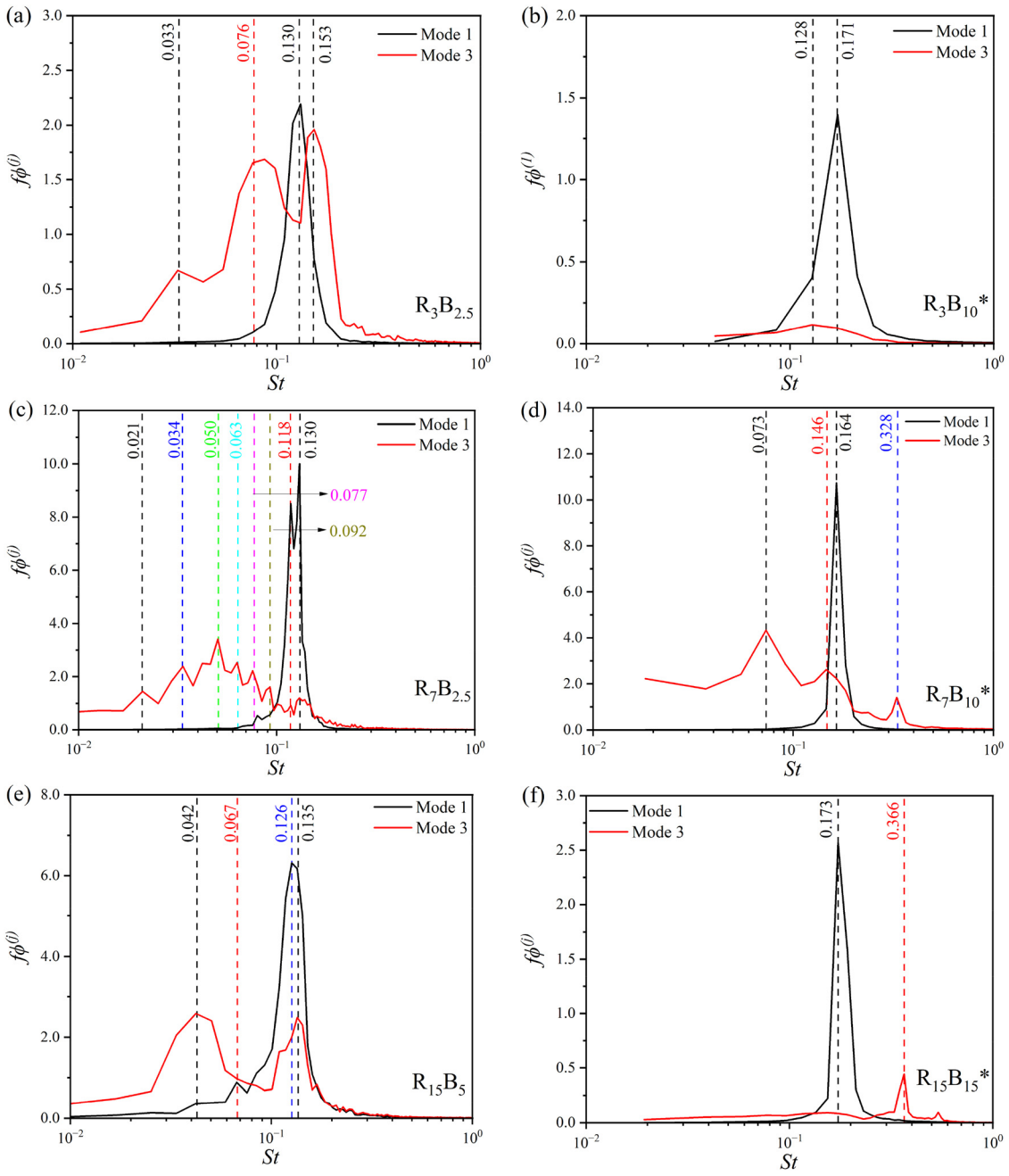


**FIG. 18.** Frequency spectra of POD modes 1 and 3 for the test cases of (a) $R_3B_{2.5}$, (b) $R_3B_{10}^*$, (c) $R_7B_{2.5}$, (d) $R_7B_{10}^*$, (e) $R_{15}B_5$, and (f) $R_{15}B_{15}^*$.

The spectra of the velocity fluctuations and POD mode coefficients show single dominant peak at the fundamental shedding frequency for the reattached test cases, but multiple peaks are observed for the unattached counterpart. The ratio of the KH to VK frequency shows more significant Reynolds number effect for prisms in the reattached regime compared to those in the unattached regime.

Distinct regions of elevated integral time scales over a wide range are observed for the unattached test cases. Additionally, the results from the two-point autocorrelation reveal that the structures are correlated over a large distance. These findings highlight the strong dynamic coupling of the separation bubbles for prisms in the unattached regime.

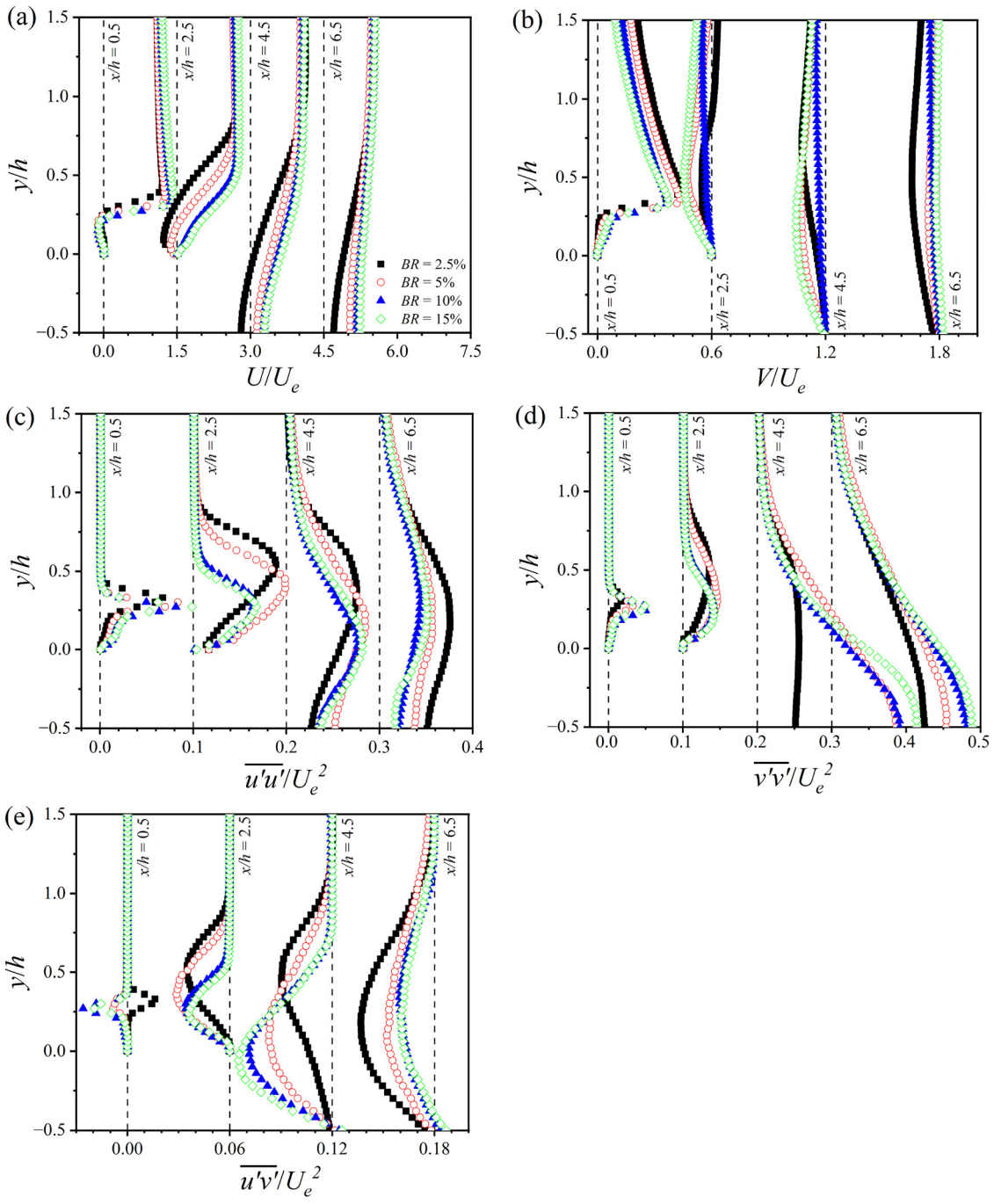


**FIG. 19.** One-dimensional profiles of the (a) streamwise mean velocity ($U$), (b) normal mean velocity ($V$), (c) streamwise ($\overline{u'u'}$) and (d) normal ($\overline{v'v'}$) Reynolds normal stresses, and (e) Reynolds shear stresses ($\overline{u'v'}$) at $x/h = 0.5$, 2.5, 4.5, and 6.5. Results are shown for all the tested blockage ratios at $\mathrm{Re} = 7500$.

Irrespective of blockage ratio or Reynolds number, the energy contributions by the normal velocity fluctuations are higher than the streamwise velocity fluctuations for the first two POD modes. The convective velocities estimated using the wavelengths of the coherent structures were 25% lower for test cases in the unattached regime. Phase portraits and the time sequences of the first two modes showed that the vortical structures are more organized for prisms in the reattached regime.

## ACKNOWLEDGMENTS

The authors are grateful for the financial support from the Natural Science and Engineering Research Council of Canada (NSERC) to Mark F. Tachie. We are also grateful to Canada Foundation for Innovation (CFI) for their invaluable support in funding the experimental facility.

## AUTHOR DECLARATIONS

### Conflict of Interest

The authors have no conflicts to disclose.

### Author Contributions

**Fati Bio Abdul-Salam:** Data curation (lead); Investigation (equal); Methodology (equal); Visualization (equal); Writing – original draft (lead). **Xingjun Fang:** Investigation (equal); Methodology (equal); Supervision (supporting); Writing – review & editing (equal). **Mark Tachie:** Conceptualization (lead); Funding acquisition (lead); Investigation (equal); Methodology (equal); Resources (lead); Supervision (lead); Writing – review & editing (equal).

## DATA AVAILABILITY

The data that support the findings of this study are available from the corresponding author upon reasonable request.

## NOMENCLATURE

| | |
|---|---|
| $BR$ | Blockage ratio |
| $d$ | Streamwise length of prism |
| FOV | Field of view |
| $h$ | Thickness of prism |
| $H$ | Water depth |
| KH | Kelvin–Helmholtz |
| $L_p$ | Reattachment length |
| $L_r$ | Recirculation length |
| PIV | Particle image velocimetry |
| POD | Proper orthogonal decomposition |
| Re | Reynolds number |
| $R_{ij}$ | Correlation |
| $S_k$ | Stokes number |
| $St$ | Strouhal number |
| $U$ | Streamwise mean velocity |
| $u'$ | Streamwise fluctuating velocity |
| $U_c$ | Convective velocity |
| $U_e$ | Incoming velocity |
| VK | von Kármán |
| $W$ | Width of channel |
| $v'$ | Normal fluctuating velocity |
| $x$ | Streamwise coordinate |
| $y$ | Normal coordinate |
| $\lambda$ | Wavelength |
| $\nu$ | Kinematic viscosity |
| $\rho_p$ | Density of seeding particles |
| $\rho_f$ | Density of water |
| $\tau$ | Integral time scale |
| $\tau_n$ | Smallest time scale |

## APPENDIX: ONE-DIMENSIONAL PROFILES OF THE MEAN VELOCITIES AND REYNOLDS STRESSES AT SELECTED STREAMWISE LOCATIONS

One-dimensional profiles of the (a) streamwise mean velocity ($U$), (b) normal mean velocity ($V$), (c) streamwise ($\overline{u'u'}$), (d) normal ($\overline{v'v'}$) Reynolds normal stresses, and (e) Reynolds shear stresses ($\overline{u'v'}$) at $x/h = 0.5$, 2.5, 4.5, and 6.5. Results are shown for all the tested blockage ratios at Re = 7500 (Fig. 19).

## REFERENCES

Alves Portela, F., Papadakis, G., and Vassilicos, J. C., "The turbulence cascade in the near wake of a square prism," J. Fluid Mech. **825**, 315–352 (2017).
Aleyasin, S. S., Tachie, M. F., and Balachandar, R., "Characteristics of flow past elongated bluff bodies with underbody gaps due to varying inflow turbulence," Phys. Fluids **33**, 125106 (2021).
Bai, H. and Alam, M. M., "Dependence of square cylinder wake on Reynolds number," Phys. Fluids **30**(1), 015102 (2018).
Bearman, P. W. and Trueman, D. M., "Investigation of flow around rectangular cylinders," Aeronaut. Q. **23**, 229–237 (1972).
Brun, C., Aubrun, S., Goossens, T., and Ravier, P., "Coherent structures and their frequency signature in the separated shear layer on the sides of a square cylinder," Flow, Turbul. Combust. **81**(1–2), 97–114 (2008).
Cermak, J. E., "Aerodynamics of buildings," Annu. Rev. Fluid Mech. **8**(1), 75–106 (1976).
Cimarelli, A., Leonforte, A., and Angeli, D., "On the structure of the self-sustaining cycle in separating and reattaching flows," J. Fluid Mech. **857**, 907–936 (2018).
Davis, R. W., Moore, E. F., and Purtell, L. P., "A numerical-experimental study of confined flow around rectangular cylinders," Phys. Fluids **27**(1), 46–59 (1984).
Durão, D. F. G., Heitor, M. V., and Pereira, J. C. F., "Measurements of turbulent and periodic flows around a square cross-section cylinder," Exp. Fluids **6**(5), 298–304 (1988).
Fang, X. and Tachie, M. F., "On the unsteady characteristics of turbulent separations over a forward–backward-facing step," J. Fluid Mech. **863**, 994–1030 (2019).
Fang, X., Tachie, M. F., and Dow, K., "Turbulent separations beneath semi-submerged bluff bodies with smooth and rough undersurfaces," J. Fluid Mech. **947**, A19 (2022).
Igarashi, T., "Characteristics of the flow around rectangular cylinders: The case of the angle of attack 0 deg," Bull. JSME **28**(242), 1690–1696 (1985).
Igarashi, T., "Fluid flow and heat transfer around rectangular cylinders (the case of a width/height ratio of a section of 2.0–4.0)," Trans. Jpn. Soc. Mech. Eng. B **52**(480), 3011–3016 (1986).
Kevin, K., Monty, J., and Hutchins, N., "Turbulent structures in a statistically three-dimensional boundary layer," J. Fluid Mech. **859**, 543–565 (2019).
Kiya, M. and Sasaki, K., "Structure of a turbulent separation bubble," J. Fluid Mech. **137**, 83–113 (1983).
Kumahor, S. and Tachie, M. F., "Turbulent flow around rectangular cylinders with different streamwise aspect ratios," J. Fluids Eng. **144**(5), 051304 (2022).
Kumahor, S. and Tachie, M. F., "Effects of streamwise aspect ratio on the spatio-temporal characteristics of flow around rectangular cylinders," Int. J. Heat Fluid Flow **101**, 109133 (2023).
Kuroda, M., Tamura, T., and Suzuki, M., "Applicability of LES to the turbulent wake of a rectangular cylinder—Comparison with PIV data," J. Wind Eng. Ind. Aerodyn. **95**(9), 1242–1258 (2007).
Lander, D. C., Moore, D. M., Letchford, C. W., and Amitay, M., "Scaling of square-prism shear layers," J. Fluid Mech. **849**, 1096–1119 (2018).
Liu, M., Kumahor, S., and Tachie, M. F., "Reynolds number effects on turbulent wakes generated by rectangular cylinders with streamwise aspect ratio between 1 to 4," J. Fluids Eng. (in press) (2023).
Lyn, D. A., Einav, S., Rodi, W., and Park, J.-H., "A laser-doppler velocimetry study of ensemble-averaged characteristics of the turbulent near wake of a square cylinder," J. Fluid Mech. **304**, 285–319 (1995).

Mashhadi, A., Sohankar, A., and Alam, M. M., "Flow over rectangular cylinder: Effects of cylinder aspect ratio and Reynolds number," Int. J. Mech. Sci. **195**, 106264 (2021).
Mohebi, M., Du Plessix, P., Martinuzzi, R. J., and Wood, D. H., "Effect of thickness-to-chord ratio on the wake of two-dimensional rectangular cylinders," Phys. Rev. Fluids **2**(6), 064702 (2017).
Moore, D. M., Letchford, C. W., and Amitay, M., "Energetic scales in a bluff body shear layer," J. Fluid Mech. **875**, 543–575 (2019a).
Moore, D. M., Letchford, C. W., and Amitay, M., "Transitional shear layers on rectangular sections," Lect. Notes Civil Eng. **27**, 519–533 (2019b).
Nakagawa, S., Nitta, K., and Senda, M., "Experimental study on unsteady turbulent near wake of a rectangular cylinder in channel flow," Exp. Fluids **27**(3), 284–294 (1999).
Norberg, C., "Flow around rectangular cylinders: Pressure forces and wake frequencies," J. Wind Eng. Ind. Aerodyn. **49**(1–3), 187–196 (1993).
Nguyen, T., Vaghetto, R., and Hassan, Y., "Experimental investigation of turbulent wake flows in a helically wrapped rod bundle in presence of localized blockages," Phys. Fluids **32**(7), 075113 (2020).
Okajima, A., "Strouhal numbers of rectangular cylinders," J. Fluid Mech. **123**, 379–398 (1982).
Park, D., and Yang, K.-S., "Flow instabilities in the wake of a rounded square cylinder," J. Fluid Mech. **793**, 915–932 (2016).
Pope, S. B., *Turbulent Flows* (Cambridge University Press, 2000).
Riches, G., Martinuzzi, R., and Morton, C., "Proper orthogonal decomposition analysis of a circular cylinder undergoing vortex-induced vibrations," Phys. Fluids **30**(10), 105103 (2018).
Robichaux, J., Balachandar, S., and Vanka, S. P., "Three-dimensional Floquet instability of the wake of square cylinder," Phys. Fluids **11**(2–3), 560–578 (1999).
Sagharichi, A., Aleyasin, S. S., and Tachie, M. F., "Turbulent separations around a slanted-back Ahmed body with square and rounded leading edge," Phys. Fluids **35**(4), 45129 (2023).
Samimy, M. and Lele, S. K., "Motion of particles with inertia in a compressible free shear layer," Phys. Fluids. A **3**(8), 1915–1923 (1991).
Sciacchitano, A. and Wieneke, B., "PIV uncertainty propagation," Meas. Sci. Technol. **27**(8), 84006 (2016).
Shadaram, A., Fard, M. A., and Rostamy, N., "Experimental study of near wake flow behind a rectangular cylinder," Am. J. Appl. Sci. **5**(8), 917–926 (2008).
Sirovich, L., "Turbulence and the dynamics of coherent structures. I: Coherent structures. II: Symmetries and transformations. III: Dynamics and scaling," Q. Appl. Math. **45**(3), 561–590 (1987).
Trias, F. X., Gorobets, A., and Oliva, A., "Turbulent flow around a square cylinder at Reynolds number 22,000: A DNS study," Comput. Fluids **123**, 87–98 (2015).
Welch, P., "The use of fast Fourier transform for the estimation of power spectra: A method based on time averaging over short, modified periodograms," IEEE Trans. Audio Electroacoust. **15**(2), 70–73 (1967).
Yoon, D.-H., Yang, K.-S., and Choi, C.-B., "Flow past a square cylinder with an angle of incidence," Phys. Fluids **22**(4), 043603 (2010).
Yu, D., Butler, K., Kareem, A., Glimm, J., and Sun, J., "Simulation of the influence of aspect ratio on the aerodynamics of rectangular prisms," J. Eng. Mech. **139**(4), 429–438 (2013).
Yu, D. and Kareem, A., "Parametric study of flow around rectangular prisms using LES," J. Wind Eng. Ind. Aerodyn. **7778**, 653–662 (1998).